Electronic Supplementary Material (ESI) for Journal of Materials Chemistry A.

Tailoring Binder-Cathode Interactions for Long-Life Room-Temperature Sodium-Sulfur Batteries

Alex Yong Sheng Eng,[a] Dan-Thien Nguyen,[a] Vipin Kumar,[a] Gomathy Sandhya Subramanian,[a] Man-Fai Ng,[b] and Zhi Wei Seh[a]*

[a] Institute of Materials Research and Engineering, Agency for Science, Technology and Research (A*STAR), 2 Fusionopolis Way, Innovis, Singapore 138634, Singapore

[b] Institute of High Performance Computing, Agency for Science, Technology and Research (A*STAR), 1 Fusionopolis Way, Connexis, Singapore 138632, Singapore

Supplementary Information

This file includes ten sections:

5. Post-Mortem Analysis of Cell Components after Extended Cycling

Figures S27-S29, and Table S7. Post-mortem analysis of cathode morphologies after long-term cycling, with various cathode binders.

Figure S30-S31, and Table S8. XPS depth profile and composition of the cycled PVDF cathode surface layer.

Figure S32 and Table S9. Post-mortem analysis of the cycled sodium anode, after long-term cycling, with various cathodes.

6. Effect of Electrolyte Additives on Stabilization of the Na Anode

Figures S33-S34. Galvanostatic strip/plating tests of sodium in symmetric cell configuration, containing various combinations of electrolyte additives.

Figure S35. Effects of individual electrolyte additive components on sodium-sulfur cell cycling.

7. Density Functional Theory Calculations for Binder-Interactions with NaSB Discharge Products

Figure S36. Optimised binding configurations and binding energies of the NaSB discharge products with different binders.

8. Battery Performance in Ether-based Electrolyte Systems

Figure S37. Cycling performances of S-PAN cathodes in ether electrolytes containing diglyme and tetraglyme solvents.

9. Flexible Cathode with Increased Sulfur Loading

Figure S38. Cycling performance of S-PAN cathodes with higher sulfur loading.

10. Performance Benchmarking for Room-Temperature Sodium-Sulfur Batteries

Gravimetric energy density calculations based on total composite weight.

Table S10. Cycle life, specific capacity, and Coulombic efficiencies for S-PAN cathodes and other recent NaSBs.

1. S-PAN composite properties

Table S1. Elemental composition of S-PAN composites based on elemental combustion analysis.

Material	Elemental composition (wt.%)			
	C	**N**	**H**	**S**
S-PAN	40.28	15.13	0.56	41.32

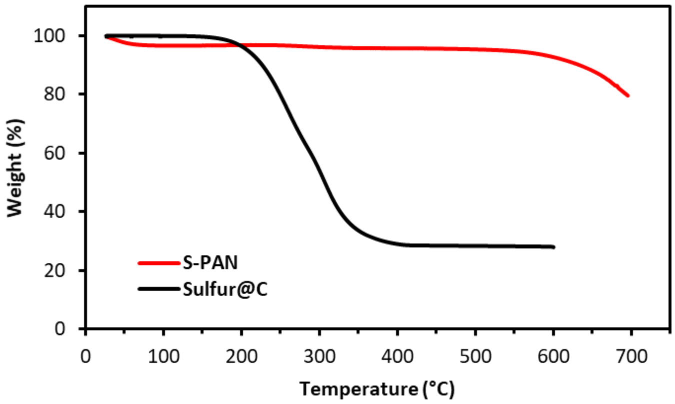

Figure S1. Thermogravimetric profiles of the S-PAN composite under nitrogen flow, as compared to typical sulfur-infiltrated carbon (*i.e.* elemental sulfur melt-diffused into porous carbon at 160 °C for 20h, followed by evaporation of residual surface sulfur at 250 °C in argon flow, denoted as Sulfur@C).

The initial weight loss step below 100 °C is very small and ascribed to the loss of adsorbed water.[1] For the sample containing elemental sulfur melt-diffused into porous carbon black (Ketjenblack), the main weight loss step above 200 °C is from the evaporation of sulfur. In comparison, no weight loss was observed for the S-PAN composite below the boiling point of elemental S_8 sulfur at 445 °C, confirming its absence. The main weight loss only begins above ~570 °C, demonstrating high thermal stability of the *short-chain* covalently-bonded sulfur species in the S-PAN composite.

2. Electrochemical sodiation and desodiation mechanisms in S-PAN

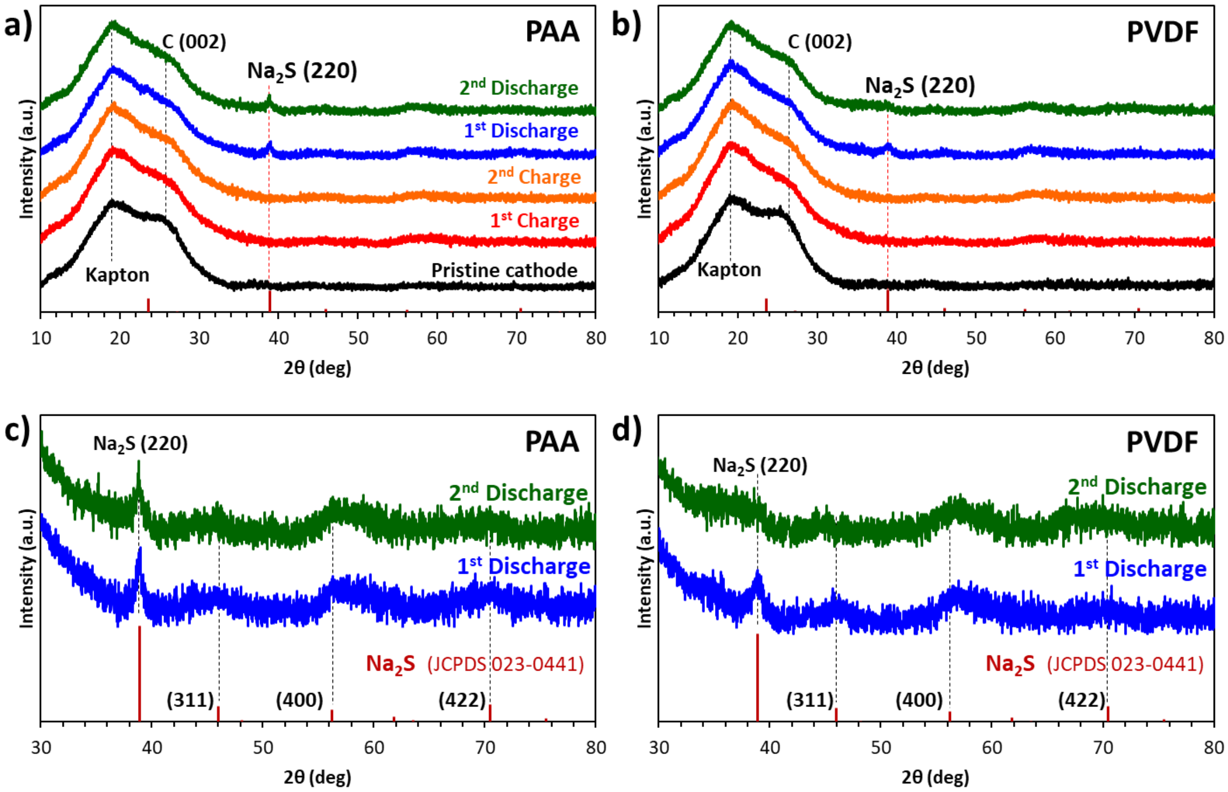

Figure S2. X-ray diffractograms of pristine and cycled S-PAN cathodes with **a)** PAA or **b)** PVDF binders. **c,d)** Enlarged XRD spectra of discharged cathodes, with sodium sulfide reference peak positions shown for comparison. Broad peak at *ca*. 19° arises from the protective Kapton polyimide film. Reference for Na_2S (JCPDS: 00-023-0441) shown for comparison. Peaks at 38.9° were observed only in the discharged states, corresponding to the prominent (220) reflection from sodium sulfide.

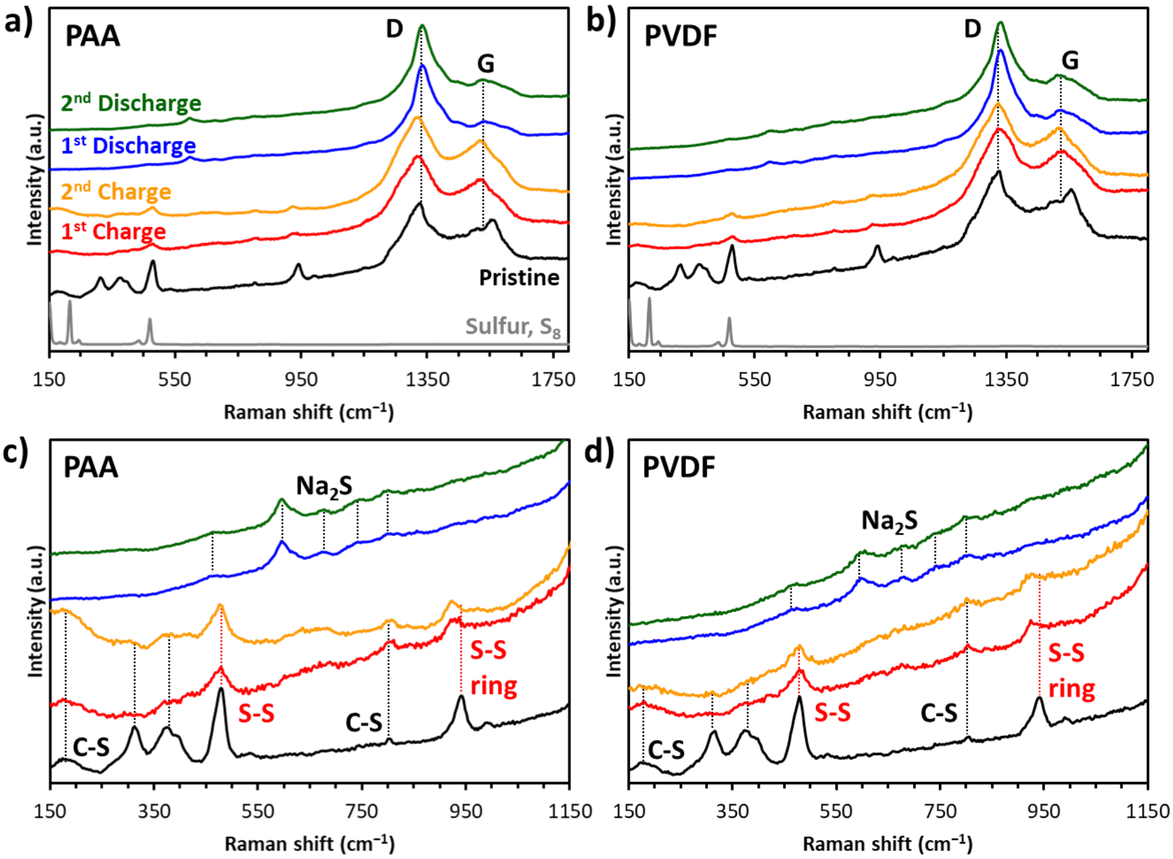

Figure S3. Raman spectra of pristine S-PAN cathodes before cycling, and after charge and discharge cycling, for cathodes containing **a)** PAA binder, **b)** PVDF binder, and **c-d)** their corresponding expanded fingerprint regions. Spectrum for elemental sulfur, S_8, also shown for reference. All spectra averaged from ten sample regions, and normalized to the D-band intensity; laser spot size <10 µm, λ_{exc} = 532 nm.

Table S2. Peak assignments for Raman spectra of pristine and cycled S-PAN cathodes in Figure S3.

Raman shift (cm^{-1})	**Assignment**	**Species**	**Observations / charge state(s)**
~1340	**D-band**	S-PAN (carbon backbone)	All
~1535	**G-band**		All
175	**C–S**	S-PAN (carbon-sulfur)	Pristine, Charged
313	**C–S** (in-plane bend)		Pristine, diminished in Charged state
375	**C–S** (deformation)		Pristine, diminished in Charged state
806	**C–S**		Pristine, broadened in Charged state
477	**S–S**	S-PAN (sulfur-sulfur)	Pristine, Charged
925	Ring stretch (**S–S** containing)		Charged
941	Ring stretch (**S–S** containing)		Pristine
460, 596, 679, 737, 806	**Na_2S**	S-PAN (Na_2S)	Discharged
153, 217, 427	**S–S** (pure S_8 ring)	Pure S_8 reference material	-

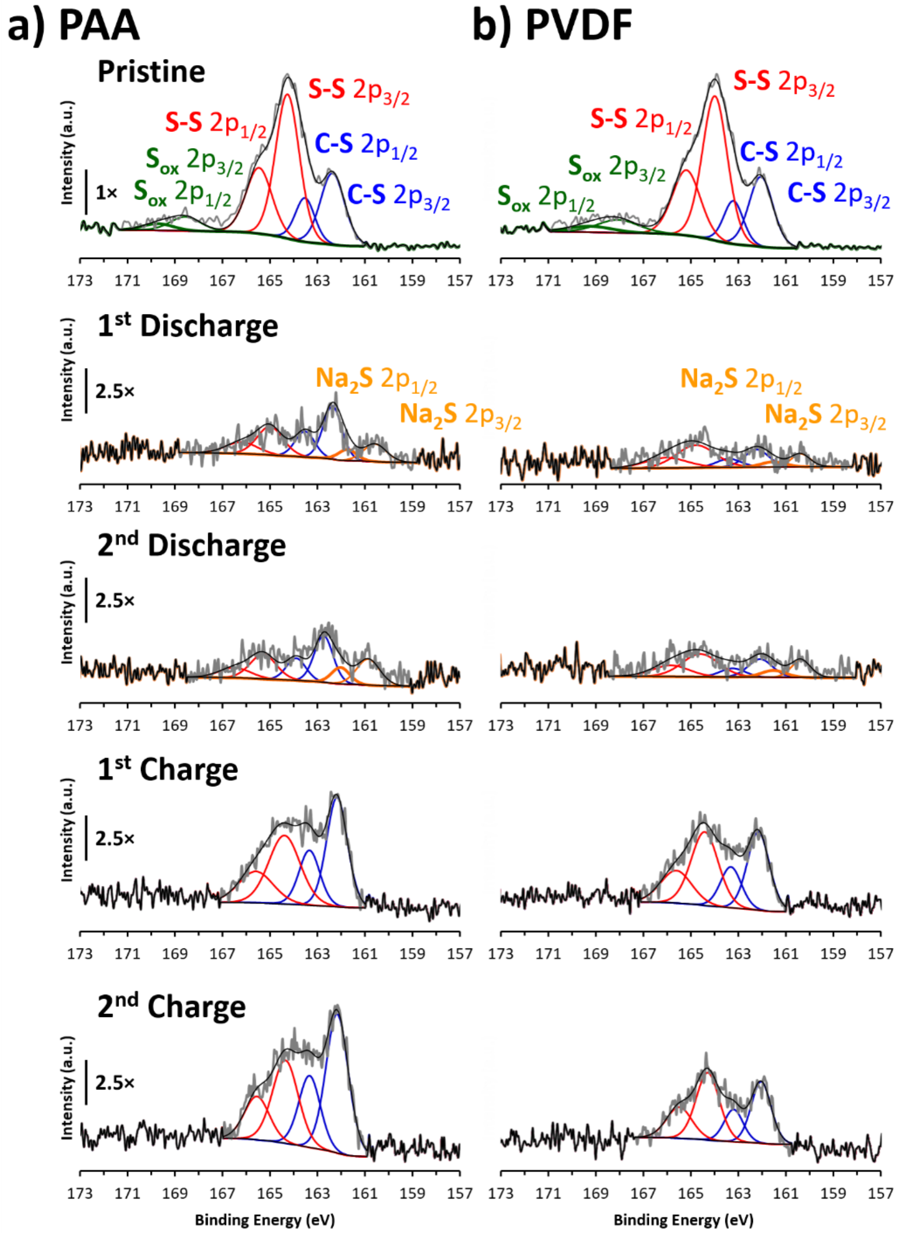

Figure S4. High resolution Sulfur-2p X-ray photoelectron spectra of S-PAN cathodes containing **a)** PAA binder (left panel) versus **b)** PVDF binder (right panel), in their pristine uncycled, charged, and discharged states after galvanostatic cycling.

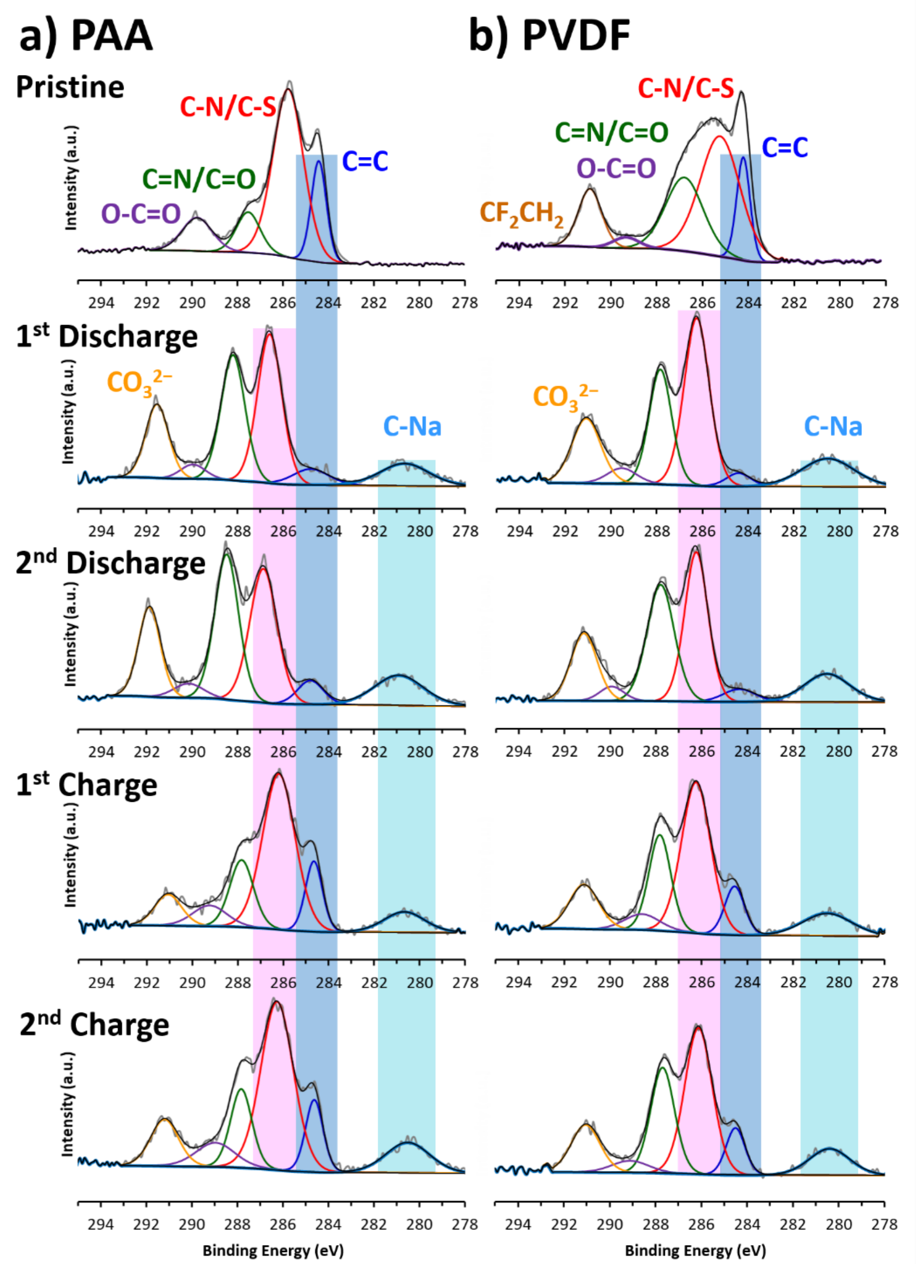

Figure S5. High resolution Carbon-1s X-ray photoelectron spectra of S-PAN cathodes containing **a)** PAA binder (left panel) versus **b)** PVDF binder (right panel), in their pristine uncycled, charged, and discharged states after galvanostatic cycling.

Table S3. Surface bonding information of sulfur and carbon species in cycled S-PAN cathodes, from deconvolution of the high resolution X-ray photoelectron spectra in Figures S4 and S5.

	Cathode Condition	**S-2p Bonding Modes (at.%)**				**C-1s Bonding Modes (at.%)**						
		Na_2S	**C–S**	**S–S**	**S_{ox}**	**C–Na**	**C=C**	**C–N/ C–S**	**C=N/ C=O**	**O–C=O**	**CH_2-CF_2**	**CO_3^{2-}**
PAA binder	**Pristine**	-	30.8	61.7	7.5	-	17.7	59.4	11.3	11.6	-	-
	1st Discharge	19.0	46.7	34.3	-	10.4	5.7	35.0	29.0	3.6	-	16.3
	2nd Discharge	32.3	41.3	26.5	-	12.7	5.4	31.4	29.9	3.7	-	16.9
	1st Charge	-	51.3	48.7	-	8.1	11.7	49.6	15.5	6.9	-	8.1
	2nd Charge	-	59.2	40.8	-	11.2	10.6	45.6	14.0	7.8	-	10.8
PVDF binder	**Pristine**	-	28.9	62.2	9.0	-	13.0	45.4	26.1	2.8	12.7	-
	1st Discharge	16.2	27.7	56.1	-	13.6	2.9	38.7	23.7	4.1	-	17.1
	2nd Discharge	20.8	27.3	51.9	-	12.0	4.0	33.4	30.4	3.4	-	16.8
	1st Charge	-	46.4	53.7	-	10.7	9.2	42.2	20.1	5.3	-	12.6
	2nd Charge	-	43.8	56.2	-	10.4	8.6	39.0	24.4	4.3	-	13.3

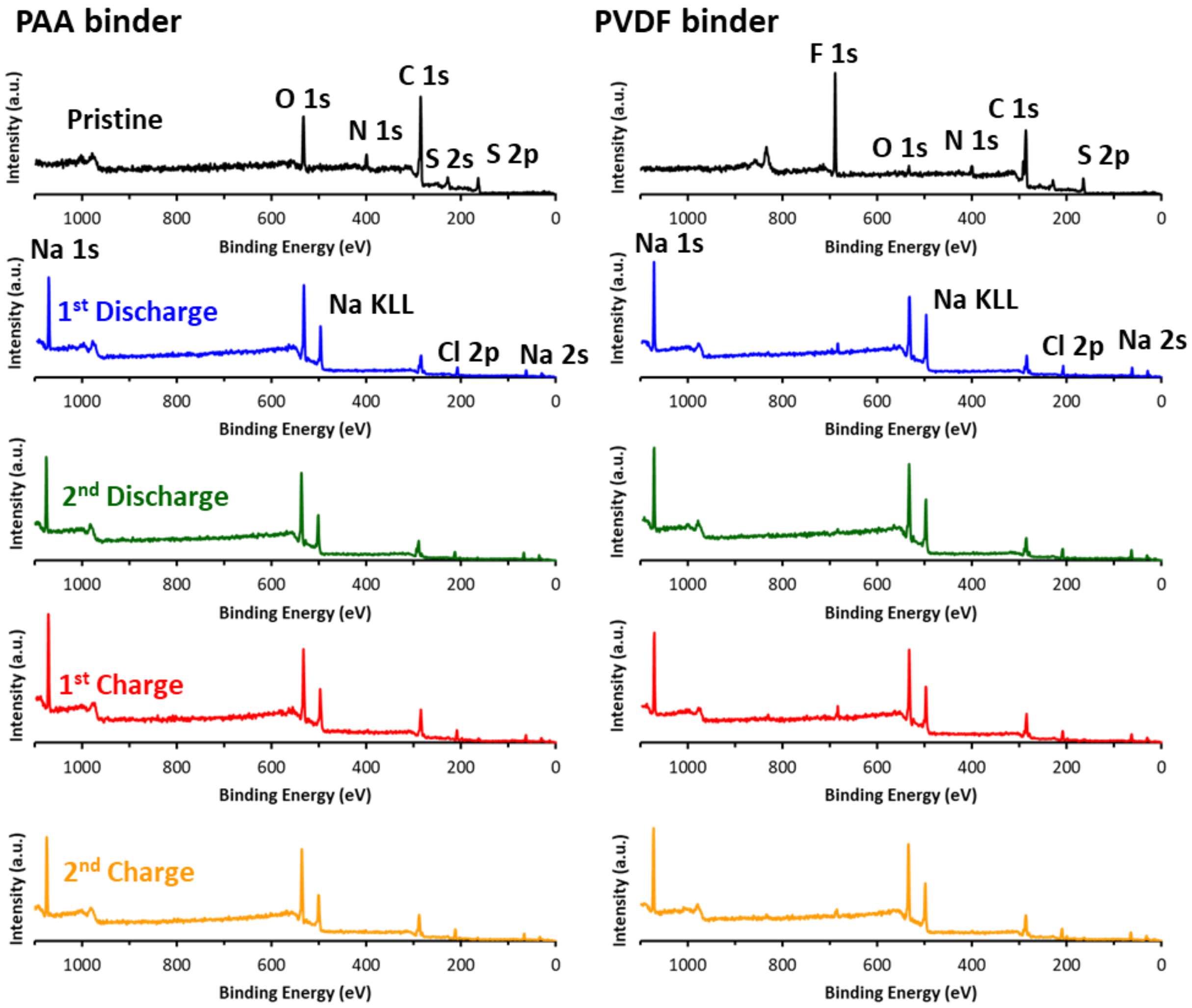

Figure S6. Wide scan X-ray photoelectron spectra of S-PAN cathodes with PAA (left panel) and PVDF binders (right panel) in the pristine state before cycling, and after charge and discharge cycling.

Table S4. Surface elemental compositions of cycled S-PAN cathodes by X-ray photoelectron spectroscopy, with either PAA or PVDF binders, in various charged and discharged states.

	Cathode Condition	**Atomic composition (at.%)**						
		C-1s	**O-1s**	**N-1s**	**S-2p**	**F-1s**	**Cl-2p**	**Na-1s**
PAA binder	**Pristine**	71.2	15.9	6.6	6.3	-	-	-
	1st Discharge	36.8	42.0	-	-	-	4.5	16.8
	2nd Discharge	34.9	42.4	-	-	-	3.6	19.2
	1st Charge	42.5	32.6	-	2.5	-	3.7	18.8
	2nd Charge	43.9	34.4	-	1.5	-	3.8	16.5
PVDF binder	**Pristine**	63.5	3.2	6.2	7.0	20.0	-	-
	1st Discharge	34.7	38.3	-	-	3.0	4.2	19.8
	2nd Discharge	33.6	41.7	-	-	1.6	4.5	18.6
	1st Charge	39.2	33.7	-	1.6	4.2	4.2	17.0
	2nd Charge	41.7	33.3	-	1.7	3.1	4.2	16.1

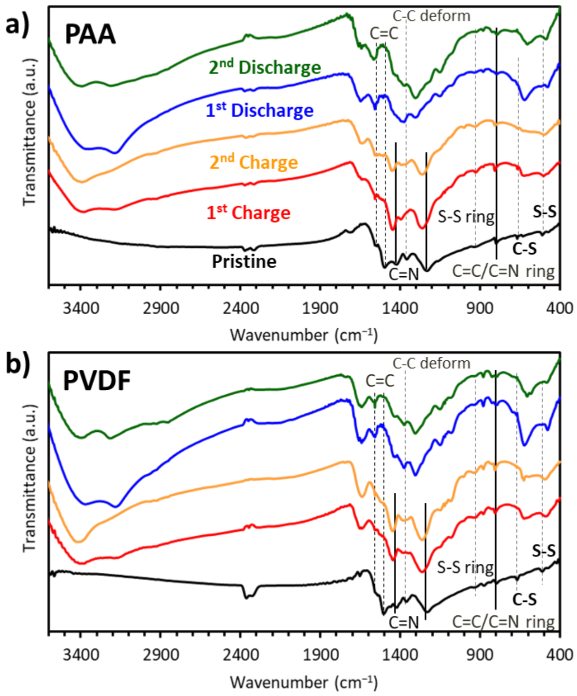

Figure S7. Fourier-transform infrared (FTIR) spectra of pristine and cycled S-PAN cathodes with **a)** PAA or **b)** PVDF binders.

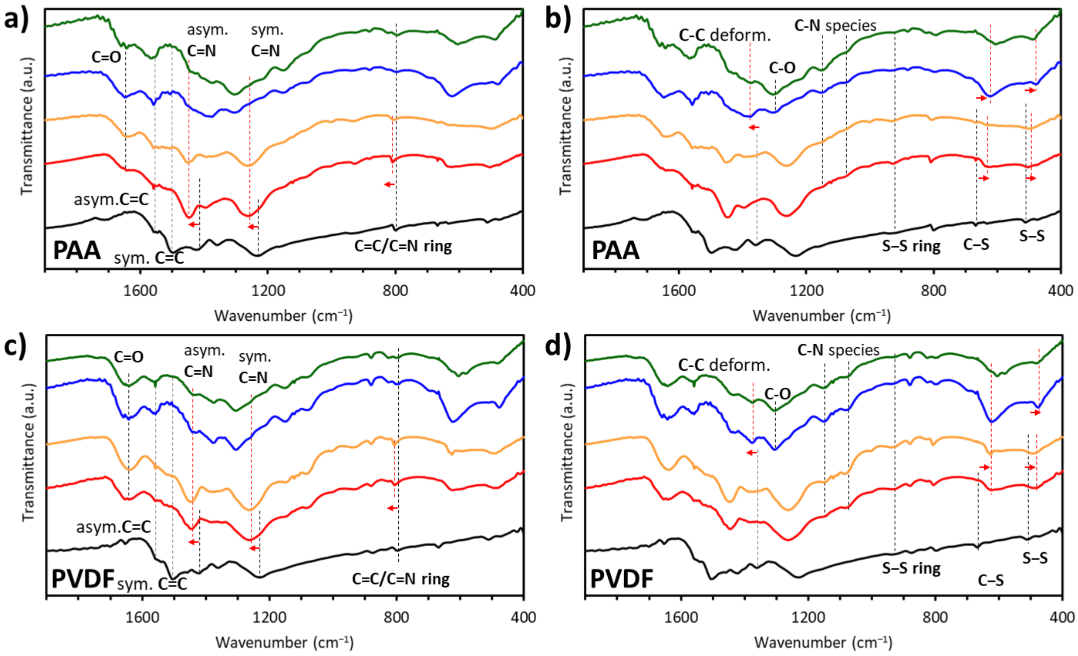

Figure S8. Enlarged FTIR spectra of pristine and cycled S-PAN cathodes with PAA or PVDF binders illustrating changes in **a,c)** double bond (C=C, C=N, C=O) vibrations and **b,d)** single bond (C-C, C-O, C-S, S-S) vibrations. Black line: pristine, red: 1st discharge, orange: 2nd discharge, blue: 1st charge, green: 2nd charge.

Table S5. Peak assignments for Fourier-transform infrared spectra of pristine and cycled S-PAN cathodes in Figure S7 and S8 above.

Wavenumber (cm^{-1})	Assignment	Observations / charge state(s)
797	Ring breath (C=N containing)	Pristine, discharged
810		Charged
1230, 1425	C=N stretches (sym, asym)	Pristine
1255, 1450		Charged, diminished in discharged states
1495	C=C stretch (symmetric)	Diminished after 1st discharge
1550	C=C stretch (asymmetric)	More prominent in discharged states
~1640	C=O stretches	Appear after 1st discharge
1355	C–C deformation	Pristine
1375	C–C deformation	More prominent in discharged states
~1300	C–O stretches	Discharged
1070, 1145	C–N/C–O stretches	More prominent in discharged states
930	Ring breath (S–S containing)	All; weak bands
~670	C–S stretch	All; shifts to lower wavenumbers after 1st discharge
~510	S–S stretch	All; shifts to lower wavenumbers after 1st discharge

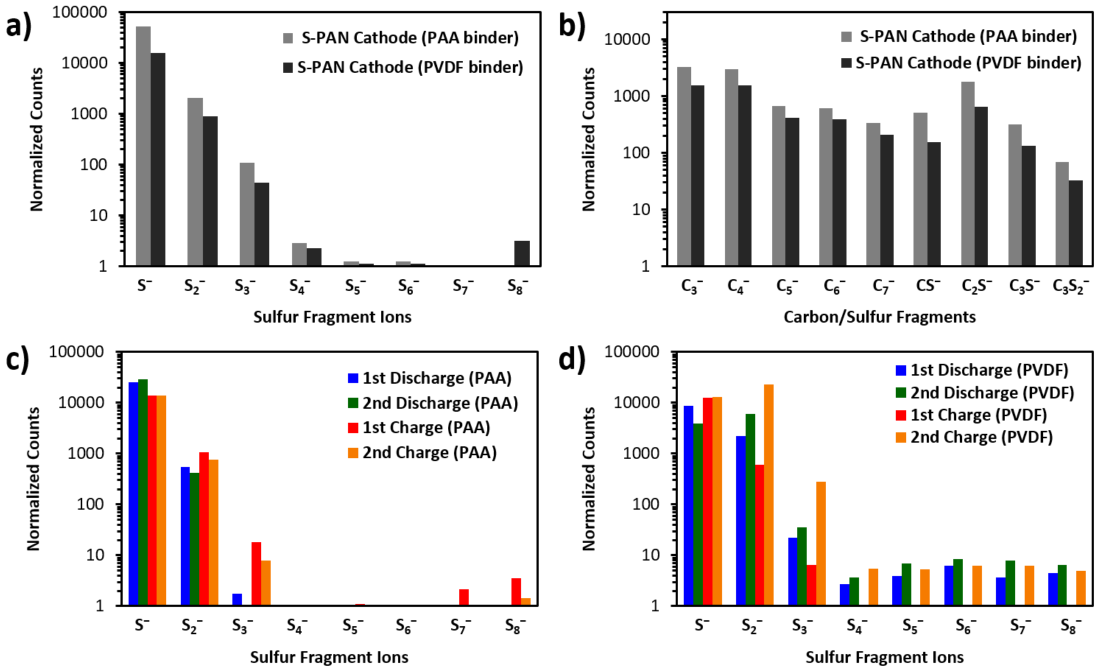

Figure S9. Distribution of **a**) sulfur fragment ions and **b**) carbon/sulfur fragments from pristine uncycled S-PAN cathodes containing either PAA or PVDF binders, obtained from time-of-flight secondary-ion mass spectrometry (TOF-SIMS). Before cycling, the vast majority of sulfur chains detected were short-chain species (*i.e.* S_x^-, where $x \leq 4$). Distribution of sulfur fragments in the charged and discharged states after galvanostatic cycling, for cathodes containing **c**) PAA binder versus **d**) PVDF binder. Note: logarithmic count scales on vertical axes.

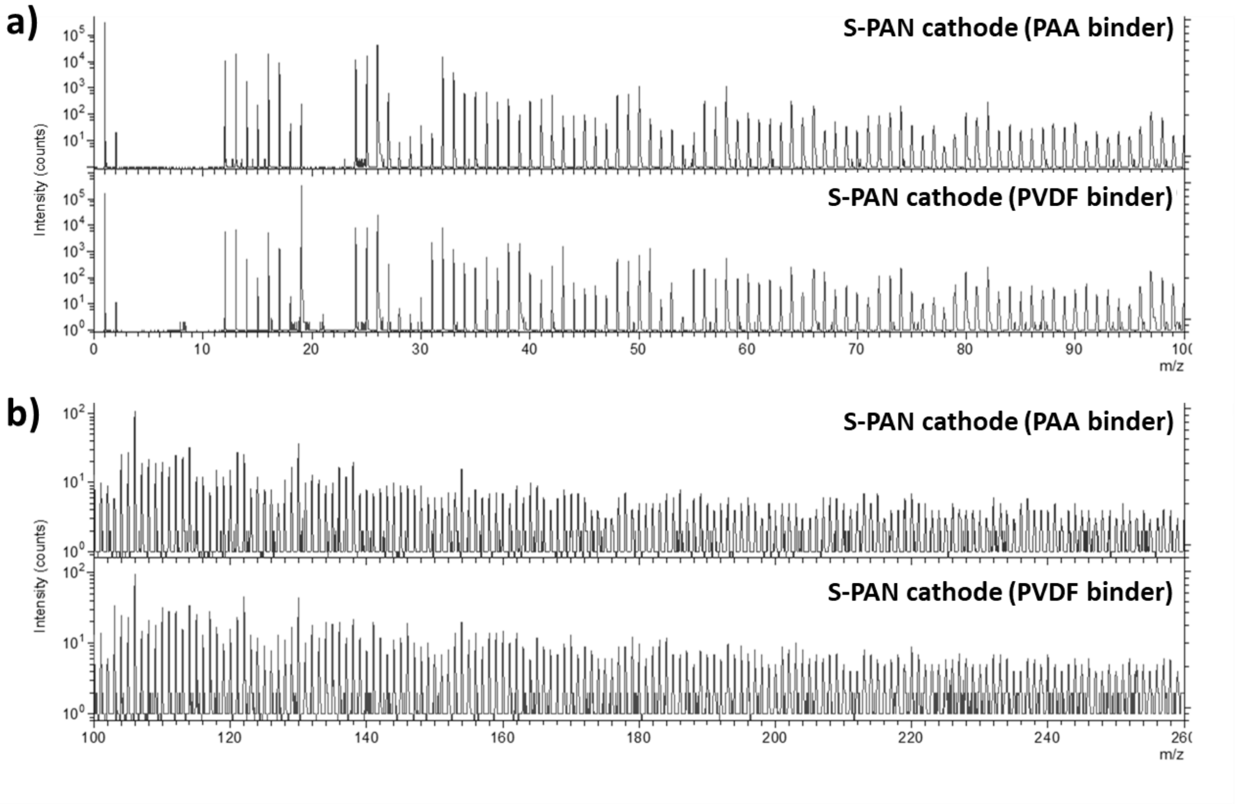

Figure S10. TOF-SIMS spectra of pristine S-PAN cathodes with PAA or PVDF binders for m/z values **a)** between 0-100, and **b)** 100-260. Note: logarithmic intensity scales.

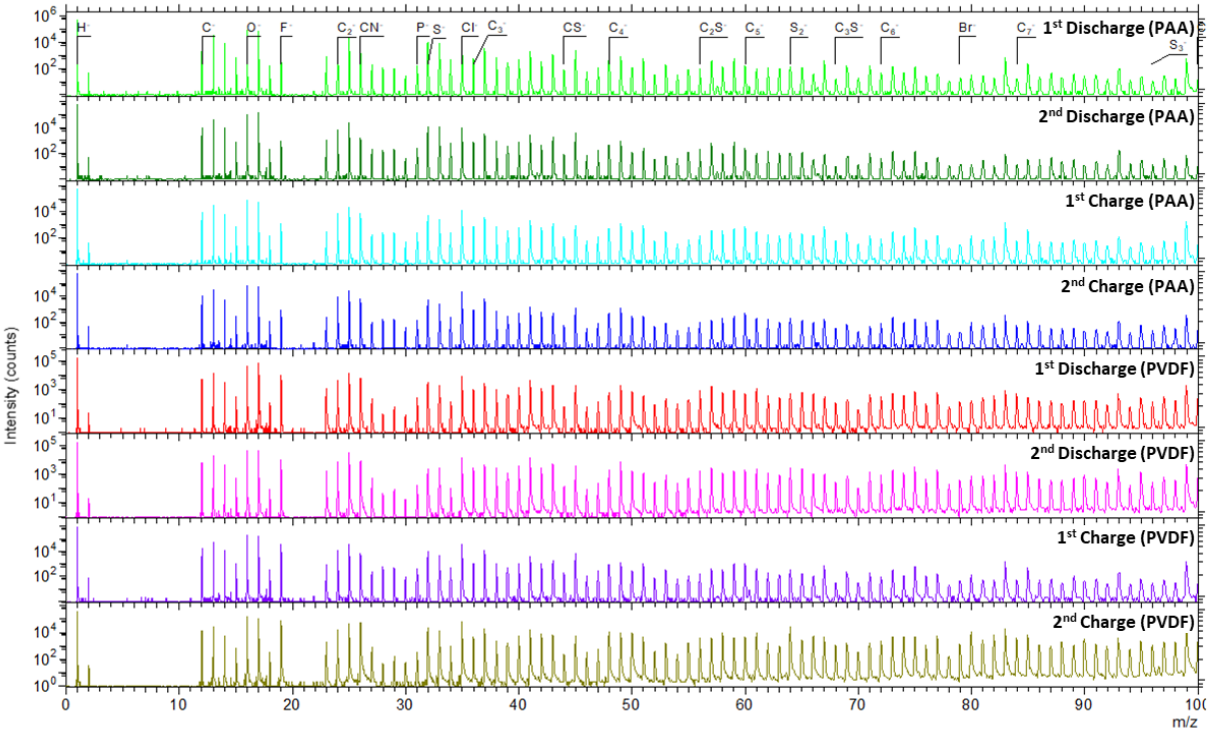

Figure S11. TOF-SIMS spectra of cycled S-PAN cathodes with PAA or PVDF binders, in various charged and discharged states, for m/z values from 0-100. Note: logarithmic intensity scales.

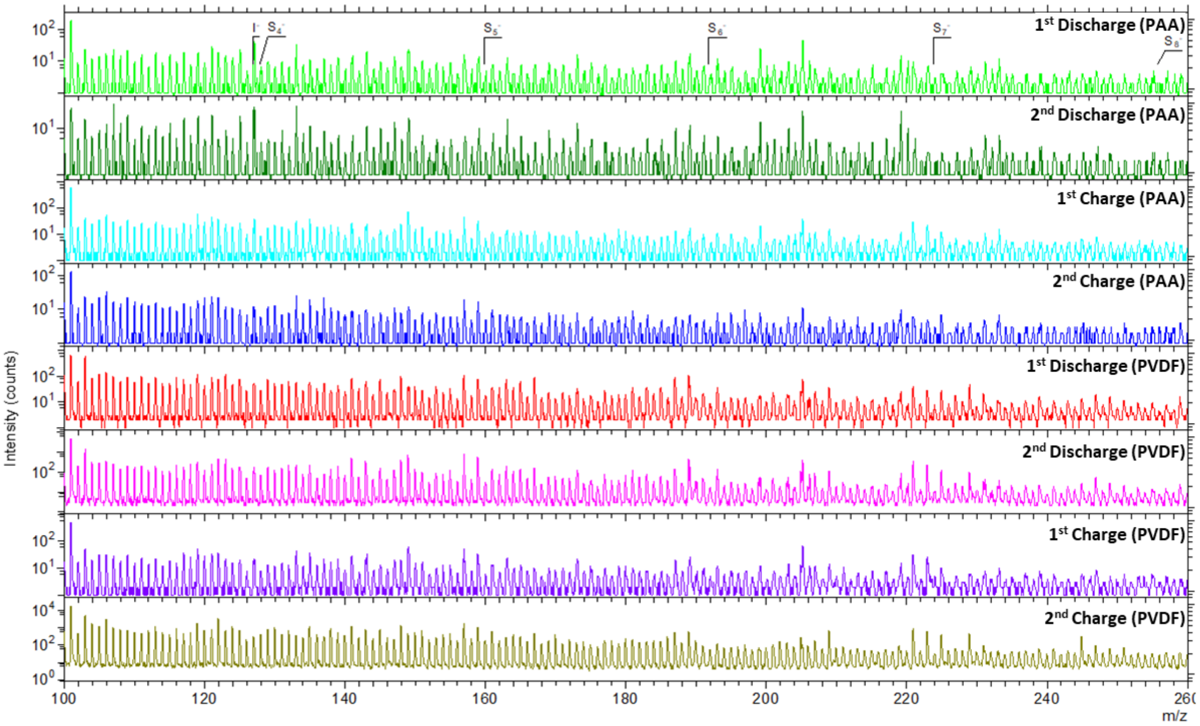

Figure S12. TOF-SIMS spectra of cycled S-PAN cathodes with PAA or PVDF binders, in various charged and discharged states, for m/z values 100-260. Note: logarithmic intensity scales.

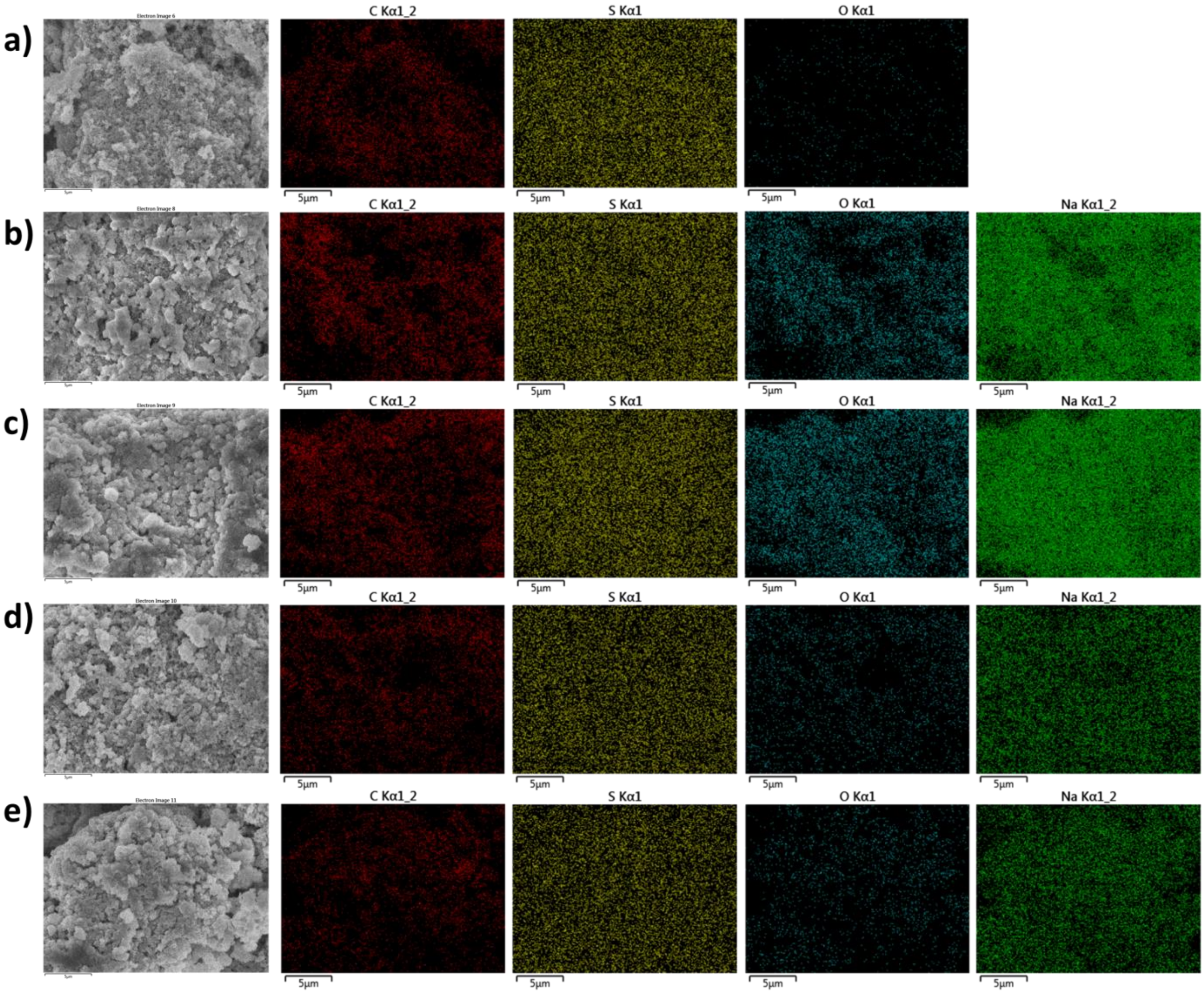

Figure S13. Scanning electron micrographs and corresponding energy dispersive X-ray maps of S-PAN cathodes with PAA binder, in **a)** pristine state prior to cycling, and after **b)** 1st discharge, **c)** 2nd discharge, **d)** 1st charge, and **e)** 2nd charge cycles.

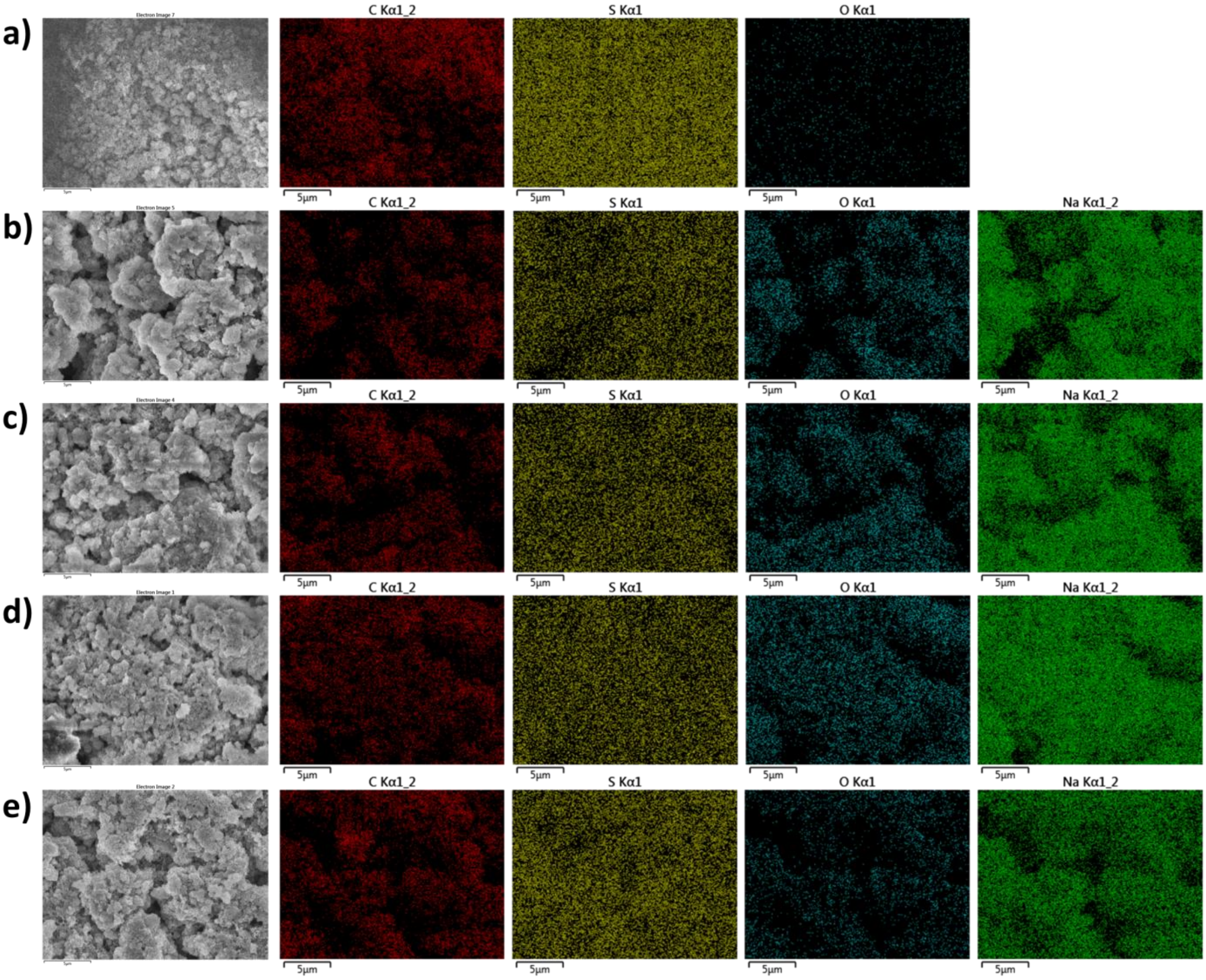

Figure S14. Scanning electron micrographs and corresponding energy dispersive X-ray maps of S-PAN cathodes with PVDF binder, in **a)** pristine state prior to cycling, and after **b)** 1st discharge, **c)** 2nd discharge, **d)** 1st charge, and **e)** 2nd charge cycles.

Table S6. Elemental composition of cycled S-PAN cathodes by energy dispersive X-ray spectroscopy, with either PAA or PVDF binders, in various charged and discharged states.

Binder	**Cathode**	**Atomic %**							**Atomic ratio**	
		C	**S**	**Na**	**O**	**N**	**F**	**Cl**	**Na/S**	**Na/C**
PAA	**Pristine**	70.2	15.4	-	1.5	12.9	-	-	-	-
	1st discharge	48.5	9.1	22.6	13.5	5.9	-	0.3	2.5	0.47
	2nd discharge	45.6	8.1	23.0	15.9	7.1	-	0.5	2.8	0.50
	1st charge	57.5	11.8	12.5	8.4	9.6	-	0.2	1.1	0.22
	2nd charge	55.5	12.6	14.0	7.5	10.0	-	0.3	1.1	0.25
PVDF	**Pristine**	72.3	13.5	-	1.1	10.6	2.5	-	-	-
	1st discharge	46.7	10.1	23.2	11.9	5.5	2.1	0.5	2.3	0.50
	2nd discharge	47.4	9.2	23.3	12.6	5.2	1.9	0.4	2.5	0.49
	1st charge	56.9	7.3	17.4	10.3	5.5	2.3	0.2	2.4	0.31
	2nd charge	57.9	10.9	12.8	6.5	8.2	3.4	0.3	1.2	0.22

3. Cycling performance of S-PAN cathodes with PAA *versus* PVDF binders

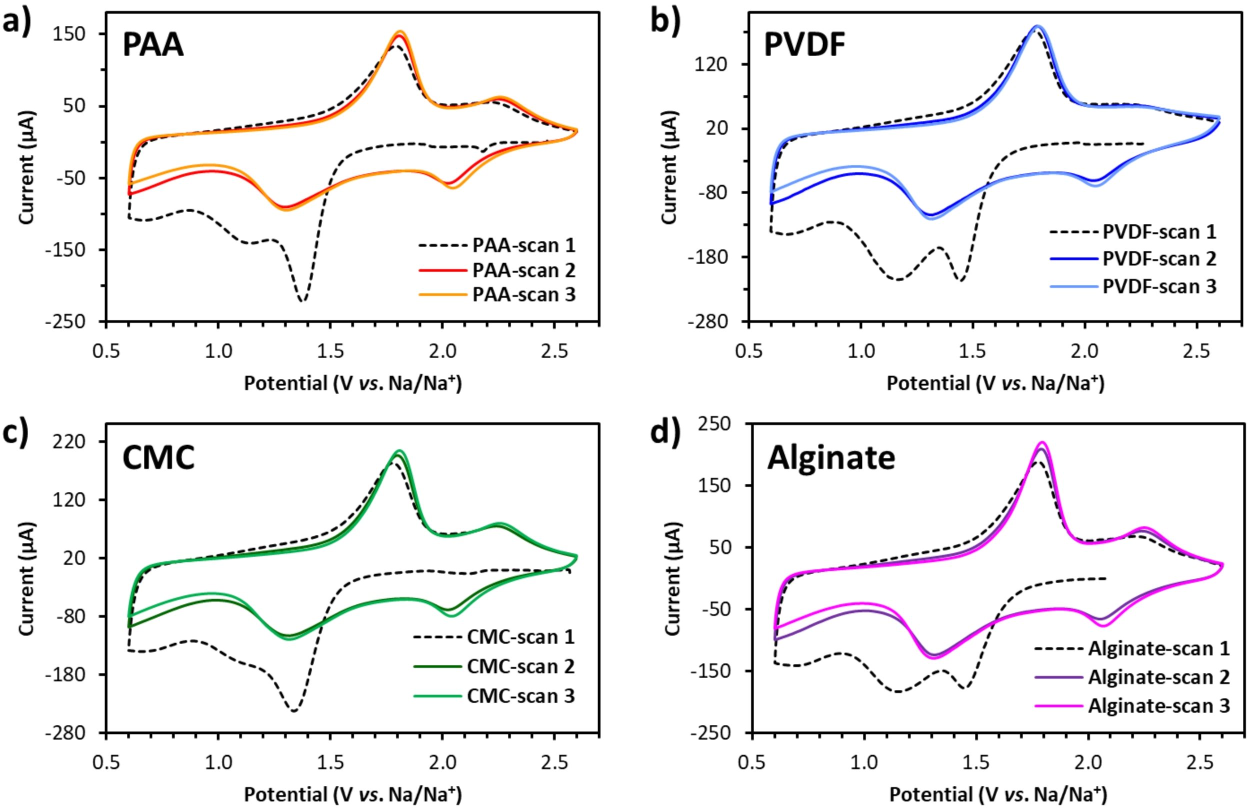

Figure S15. Cyclic voltammograms of sodium-sulfur cells with S-PAN cathodes containing **a)** PAA, **b)** PVDF, **c)** CMC, or **d)** alginate binder, at a slow scan rate of 0.05 mV s^{-1} for the first three cycles. Initial scan conducted in cathodic direction (discharge) starting from open circuit potential, and ending at 2.6 V *vs*. Na/Na^+. Diminished oxidation peaks at *ca*. 2.3 V were observed only in cathodes containing PVDF as binder.

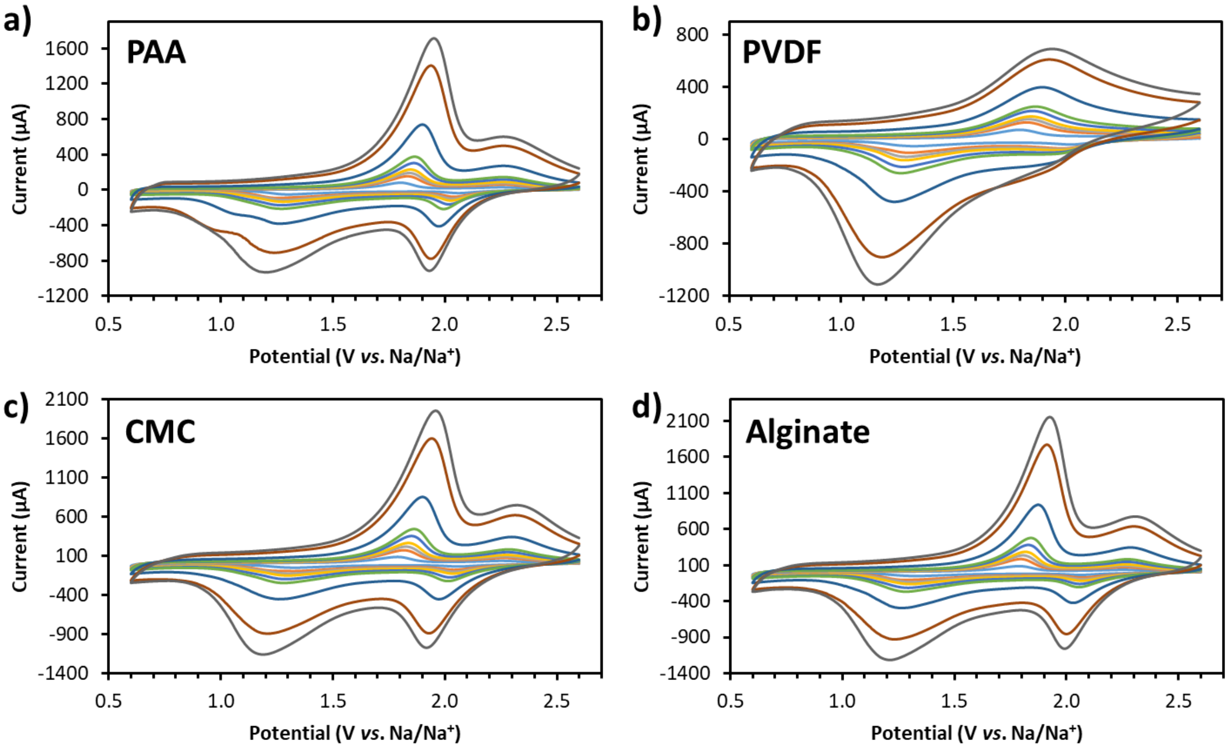

Figure S16. Cyclic voltammograms at varying scan rates with S-PAN cathodes containing **a)** PAA, **b)** PVDF, **c)** CMC, or **d)** alginate binder, over a large range of scan rates from 0.02 mV s^{-1} to 0.5 mV s^{-1}.

In PVDF-containing cathodes, the peak currents of the redox pair at higher potentials (*i.e.* oxidation at *ca*. 2.3 V and reduction at *ca*. 2.0 V *vs*. Na/Na$^+$) are progressively diminished at increasing scan rates, indicating either a slow mechanistic process or mass transfer limitation. This redox pair corresponds to the sodium polysulfide to sulfur ($Na_2S_x \rightleftharpoons S_x$) conversion.

However, as the active material is fixed throughout, it follows that its redox mechanism must certainly remain unchanged, regardless of the binder present. Hence, the possibility of mechanistic differences can be excluded. The disappearance of the redox pair can therefore be attributed to limitations in mass transfer (*i.e.* Na$^+$ ion diffusion) within the electrode, due to differences in the surrounding chemical environment as a result of the binder.

Due to the gradual disappearance of the discussed peaks at 2.3 V and 2.0 V in the PVDF system with increasing scan rate, the more prominent cathodic peak at *ca*. 1.2 V and anodic peak at *ca*. 1.85 V for the sodium sulfide-polysulfide ($Na_2S \rightleftharpoons Na_2S_x$) conversion were used instead in the determination of kinetic parameters from cyclic voltammetry, as shown below in Figures S17-S19.

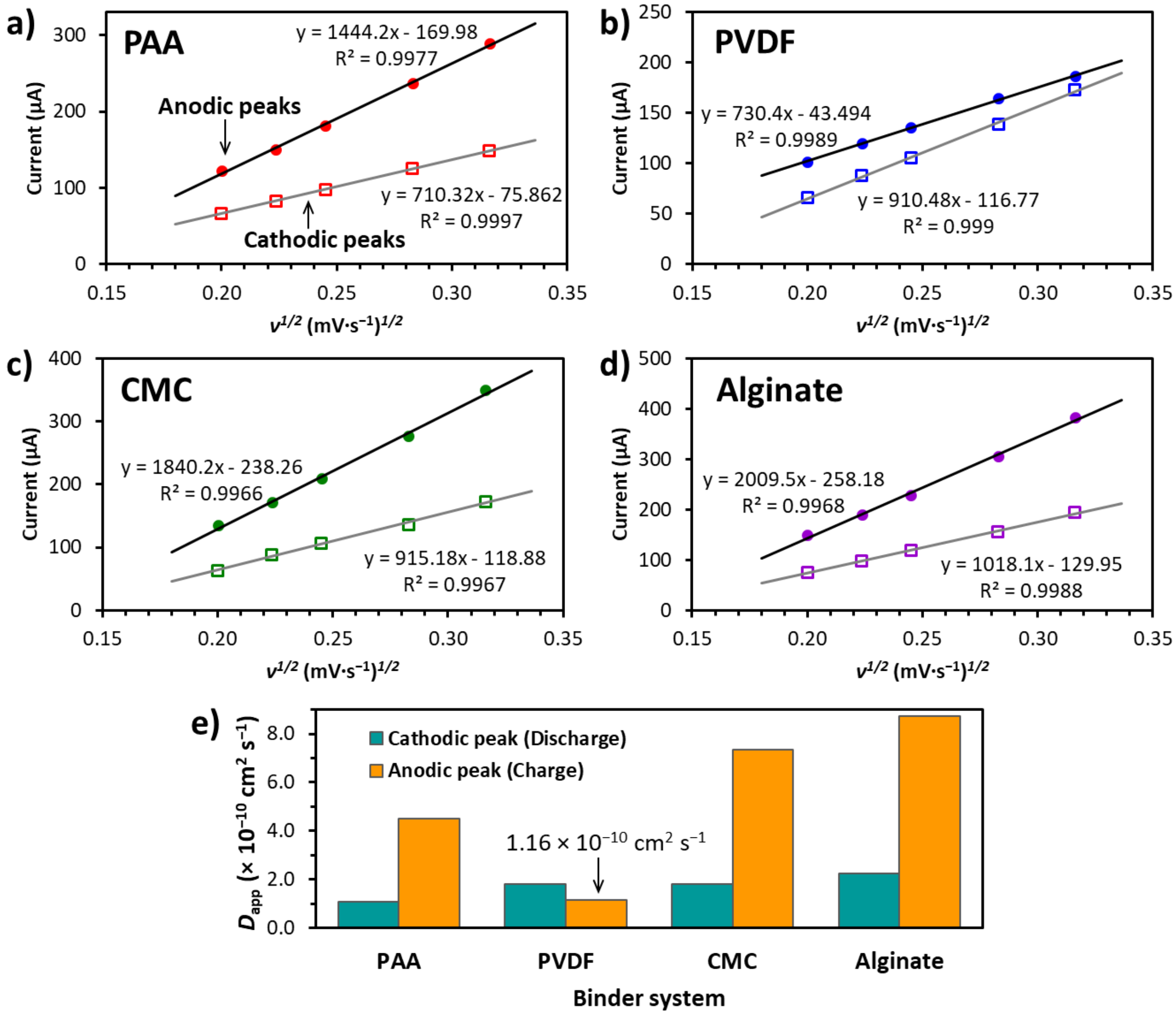

Figure S17. Plots of anodic (black lines, solid circles) and cathodic (grey lines, hollow squares) peak currents versus the square root of the voltammetric scan rate, for S-PAN cathodes containing **a)** PAA, **b)** PVDF, **c)** CMC, or **d)** alginate binder, within a linear region of scan rate values (0.04 mV s^{-1} to 0.1 mV s^{-1}). The anodic and cathodic peaks refer to the main oxidation at *ca*. 1.85 V and reduction at *ca*. 1.2 V *vs*. Na/Na^+ respectively. **e)** Calculated values of the apparent Na^+ ion diffusion coefficient (D_{app}) for the cathodic process (*i.e.* cell discharge) and anodic process (*i.e.* cell charge), in the four binder systems.

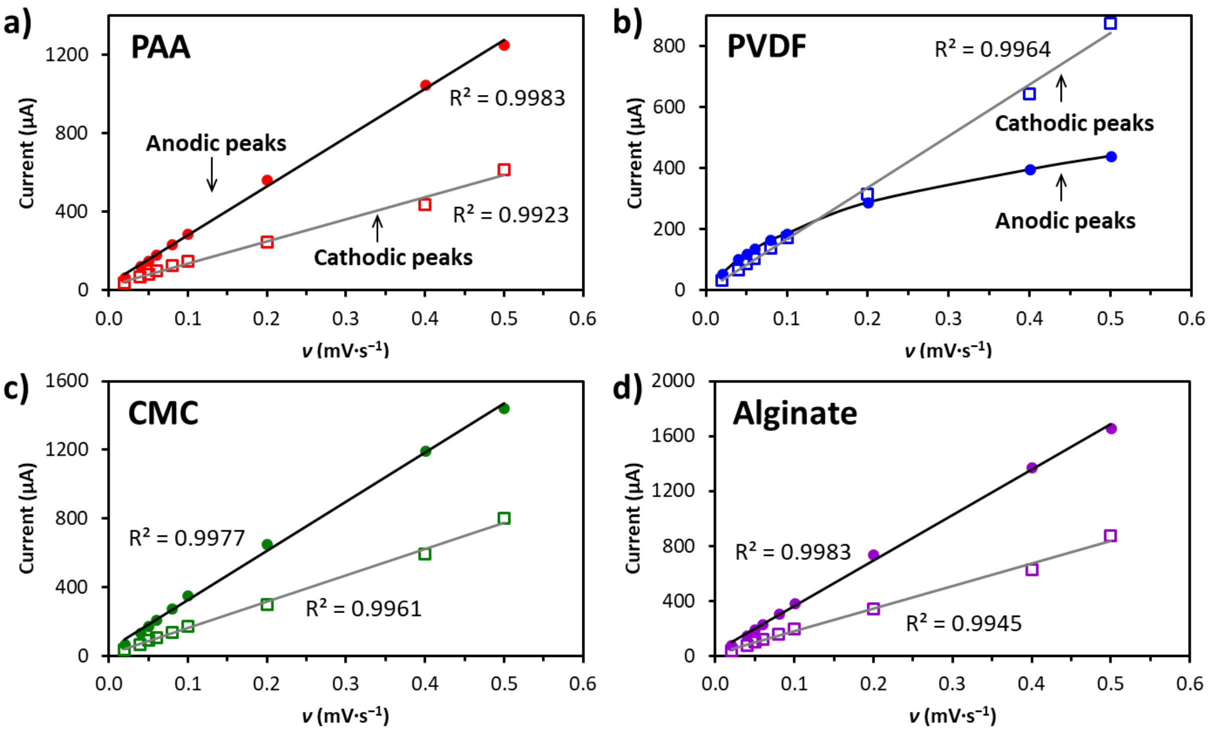

Figure S18. Linear regression plots of anodic (black lines, solid circles) and cathodic (grey lines, hollow squares) peak currents versus the voltammetric scan rate, for S-PAN cathodes containing **a)** PAA, **b)** PVDF, **c)** CMC, or **d)** alginate binder. Extended scan rate range: 0.02 mV s^{-1} to 0.5 mV s^{-1}.

High levels of linearity were observed in all instances, with the exception of the anodic peak current in the PVDF binder system, indicating mass transfer limitations at high scan rates.

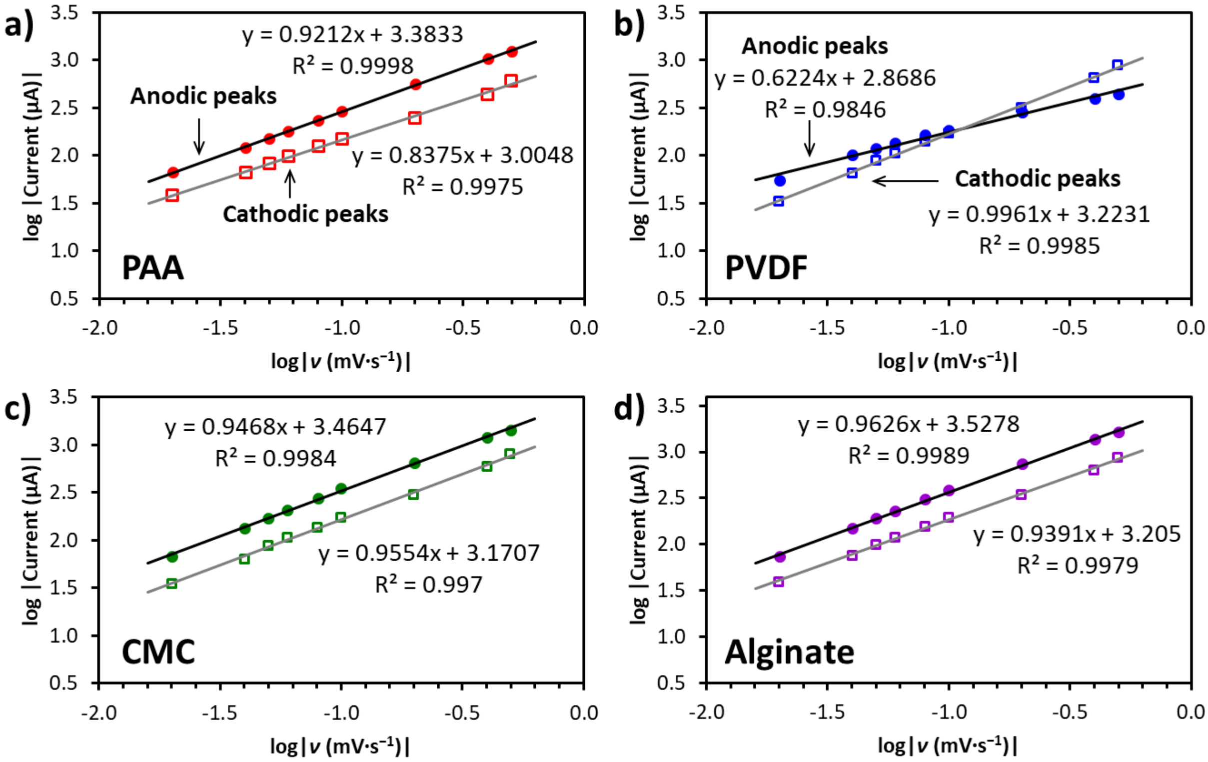

Figure S19. Double logarithmic plots of the primary oxidation and reduction peak currents versus the voltammetric scan rate, for S-PAN cathodes containing **a)** PAA, **b)** PVDF, **c)** CMC, or **d)** alginate binder. Scan rate range: 0.02 mV s^{-1} to 0.5 mV s^{-1}. Anodic and cathodic peaks refer to the main oxidation at *ca*. 1.85 V and reduction at *ca*. 1.2 V *vs*. Na/Na$^+$ respectively.

The gradient of the double logarithmic plot ($0.5 \leq m \leq 1.0$) provides an estimate of the relative contributions of diffusion control versus surface-confined mass transfer processes (where pure diffusion control: $m = 0.5$, pure surface-confined process: $m = 1$). The anodic process for the conversion of sodium sulfide to sodium polysulfide ($Na_2S \rightarrow Na_2S_x$) in PVDF-based cathodes is thus observed to be particularly slow.

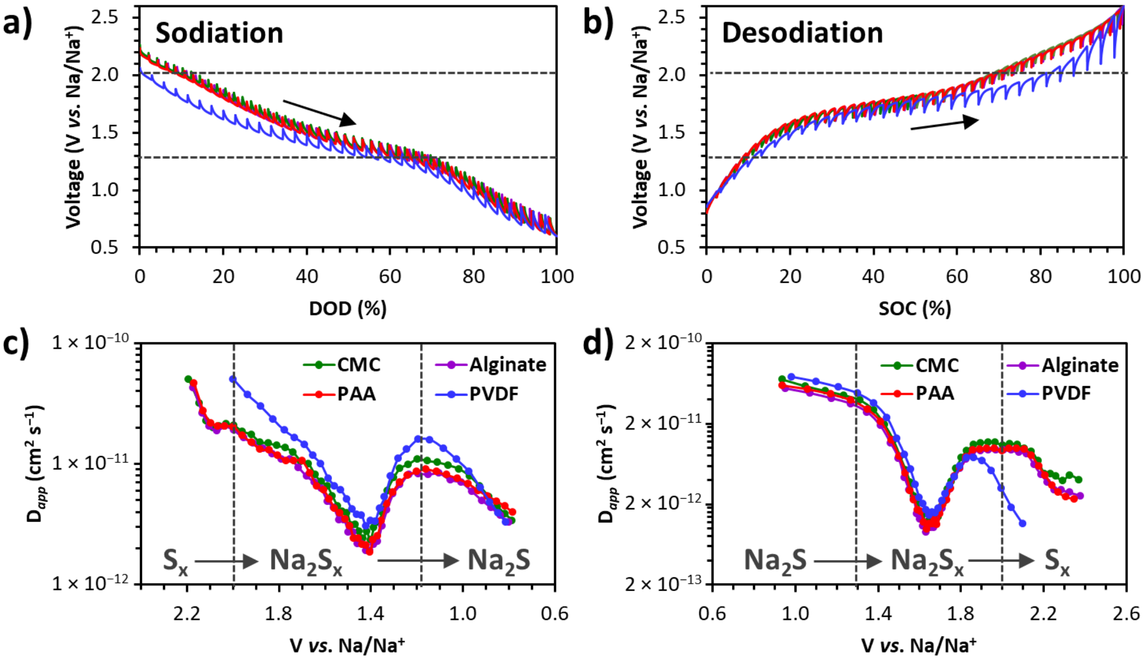

Figure S20. **a,b)** Galvanostatic intermittent titration technique (GITT) analysis of S-PAN cathodes with all tested binders (PAA: red line, PVDF: blue line, CMC: green line, alginate: purple line). Conditions: 5 min galvanostatic pulses at 0.2 C, followed by 2 h relaxation times. Diffusion coefficients as a function of cell potential for the **c)** discharge/sodiation and **d)** charge/desodiation processes.

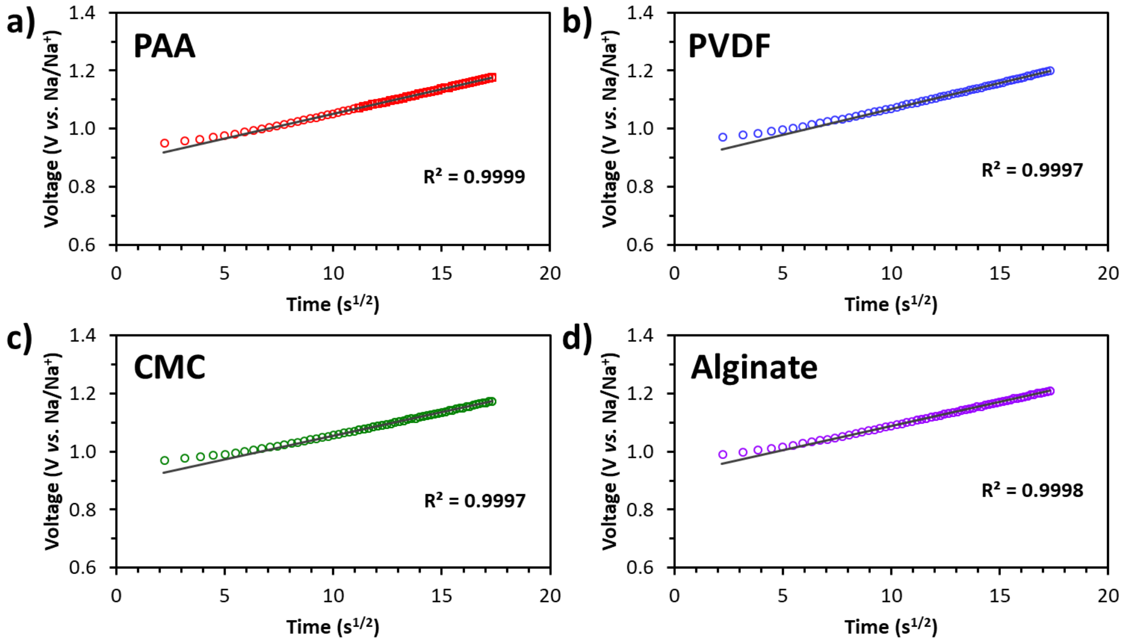

Figure S21. Plots of the potential versus the square root of the duration of the titration current pulse during the GITT charging process for the various cathodes, demonstrating good linearity of dE/dvt for accurate determination of diffusion coefficients from GITT.

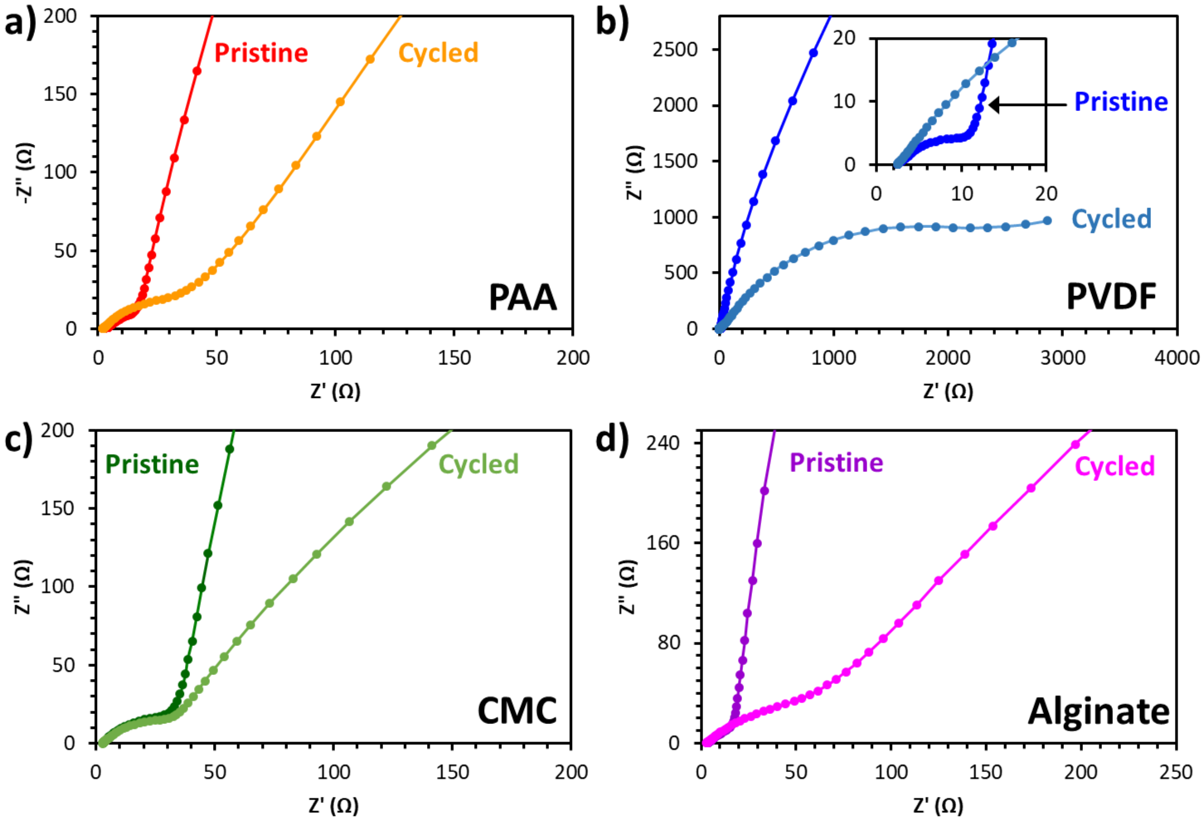

Figure S22. Electrochemical impedance Nyquist plots of sodium-sulfur cells with S-PAN cathodes containing **a)** PAA, **b)** PVDF, **c)** CMC, or **d)** alginate binder at open circuit potential *before* cycling and after voltammetric cycling between 0.6 V and 2.6 V *vs*. Na/Na$^+$ for three cycles and ending in the charged state. Conditions: A.C. perturbation: 5 mV, frequency range: 1 MHz to 0.01 Hz.

4. Long-term battery cycling effects in different binders

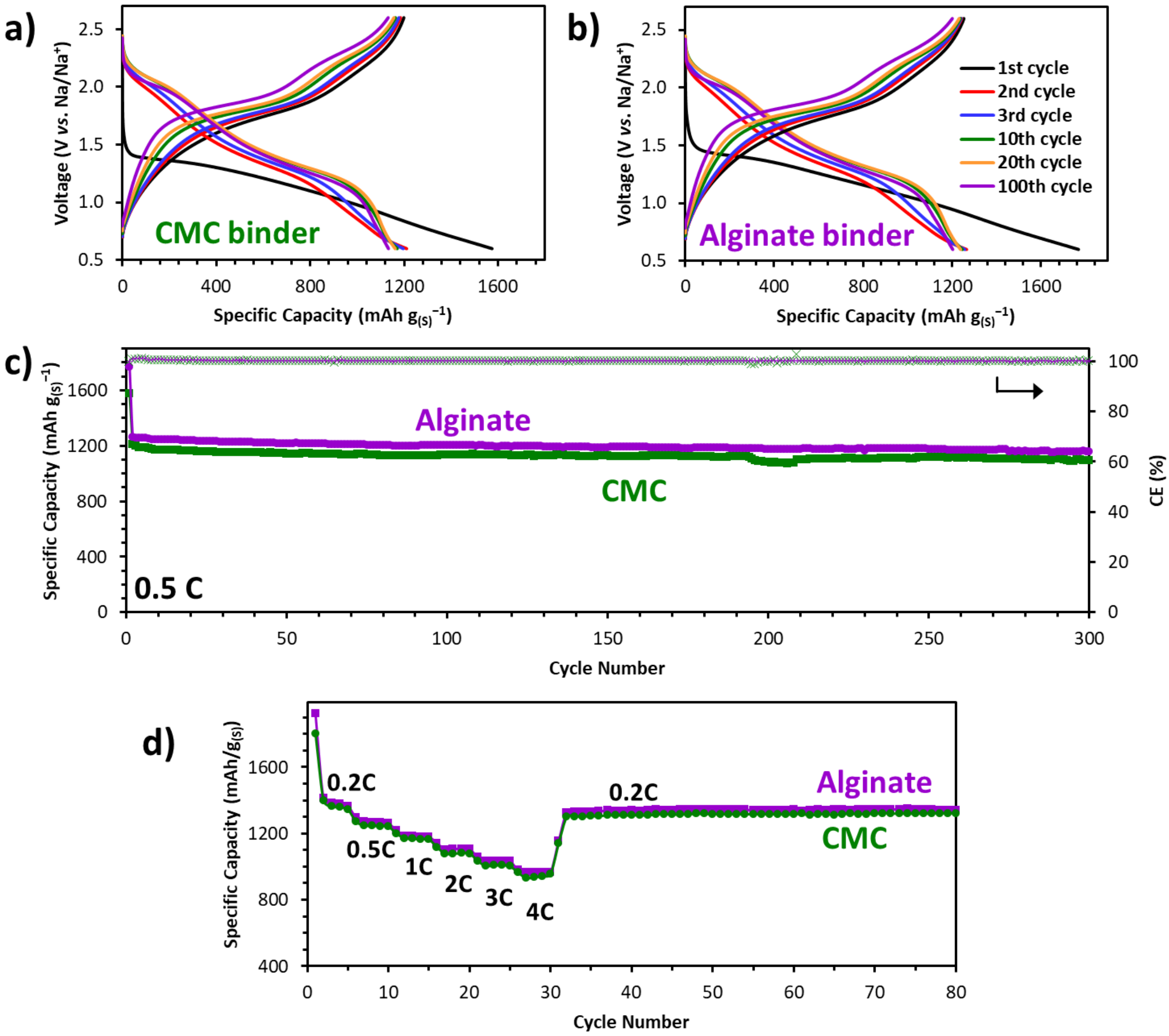

Figure S23. Performances of other carboxyl-containing binders. Galvanostatic charge/discharge profiles of S-PAN cathodes containing naturally-derived **a)** sodium carboxymethyl cellulose (CMC) or **b)** sodium alginate binders (Sigma-Aldrich; 10 wt.%), with a 1 M NaClO$_4$ electrolyte in EC:DMC (1:1 v/v) containing 40 mM SnCl$_2$ and 8 vol.% FEC additives. Legend: 1st cycle: black, 2nd cycle: red, 3rd cycle: blue, 10th cycle: green, 20th cycle: orange, 100th cycle: purple. **c)** Galvanostatic cycling performance and Coulombic efficiencies at 0.5 C. **d)** Rate performance for CMC and alginate cathodes.

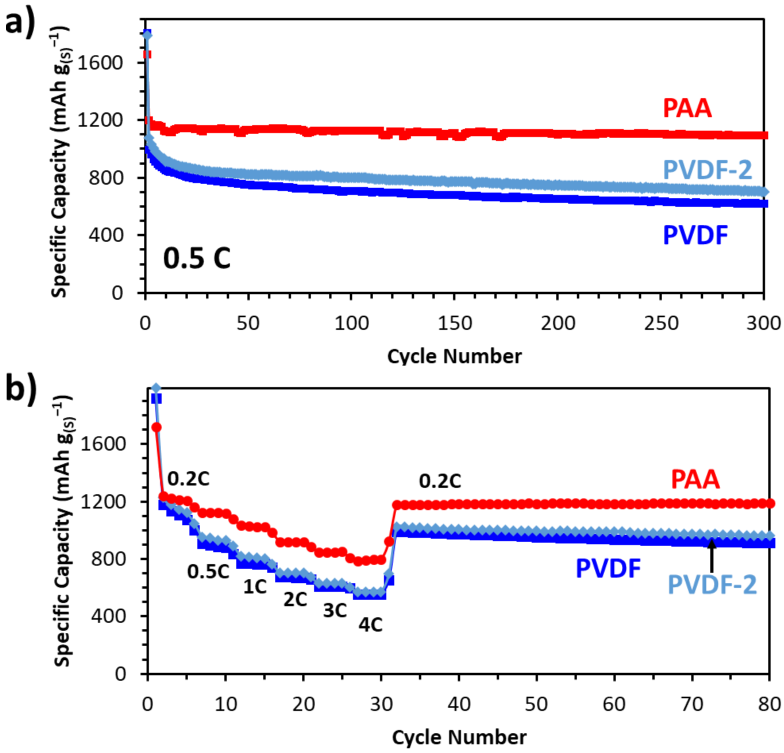

Figure S24. Comparison of PAA binder with PVDF binders of varying molecular weight. a) Galvanostatic cycle performance, and **b)** rate performance of S-PAN cathodes containing 10 wt.% binders: *(1)* PAA (avg. M_w = 450k, Sigma-Aldrich), *(2)* PVDF (avg. M_w = 534k, Sigma-Aldrich), and *(3)* PVDF-2 (avg. M_w = 1.0–1.1 M, Solvay), with a 1 M $NaClO_4$ electrolyte in EC:DMC (1:1 v/v) containing 40 mM $SnCl_2$ and 8 vol.% FEC additive.

The PVDF binder with higher molecular weight (Solef® 5130, Solvay, Belgium) exhibited similar rate performances, and only marginally higher capacity retention with cycling. Both PVDF cathodes exhibited a similar trend where most of their capacity loss occurred during the early stages of cycling (<20 cycles, Figure S24a).

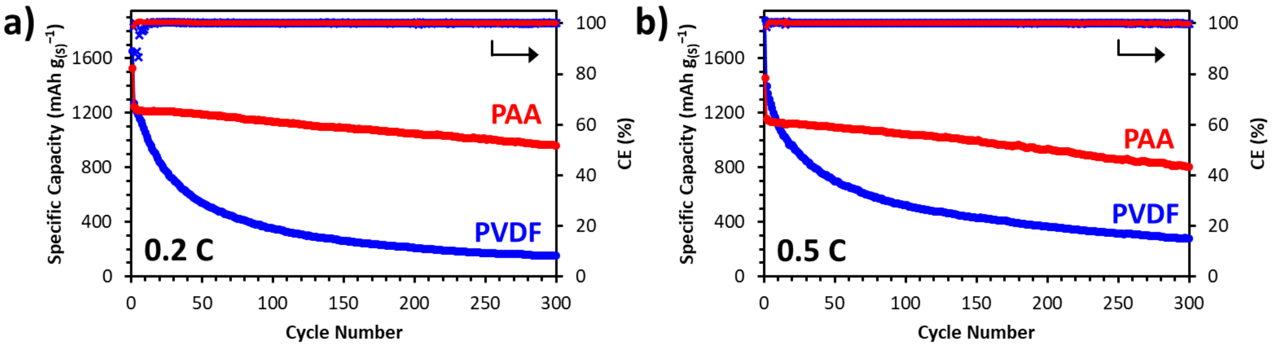

Figure S25. Galvanostatic cycle performance and Coulombic efficiencies of S-PAN sodium-sulfur cells at **a)** 0.2 C and **b)** 0.5 C, *without* electrolyte additives; 1 M $NaClO_4$ in EC:DMC.

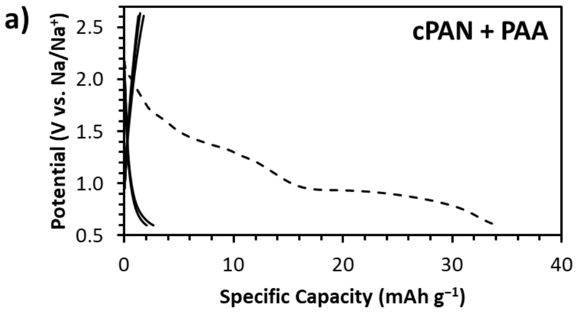

b)

	Elemental composition (wt.%)			
	C	**H**	**N**	**S**
cPAN	66.8	4.3	20.5	0.0

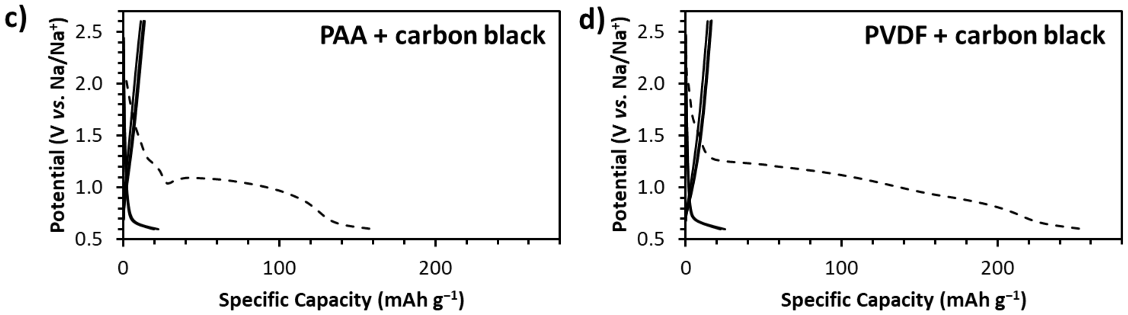

Figure S26. a) Galvanostatic charge/discharge profiles of carbonized PAN (cPAN) cathodes, without sulfur, at current density of 0.2 A g^{-1}. **b)** Elemental composition of cPAN by elemental combustion analysis demonstrating absence of sulfur. Charge/discharge profiles of carbon black (Super P) cathodes (90 wt.%), with 10 wt% **c)** PAA and **d)** PVDF binders at 0.2 A g^{-1}. First five cycles shown; dotted lines represent first discharge cycle.

Lower-voltage discharge plateaus were observed to occur during the first discharge process and contributed to an irreversible capacity for all cathode compositions, and regardless of the presence of either electrolyte additive. This phenomenon is primarily caused by the reduction of carbonate electrolyte solvents on the pristine electrode surface in forming the solid electrolyte interphase.[2-4]

5. Post-mortem analysis of cell components after extended cycling

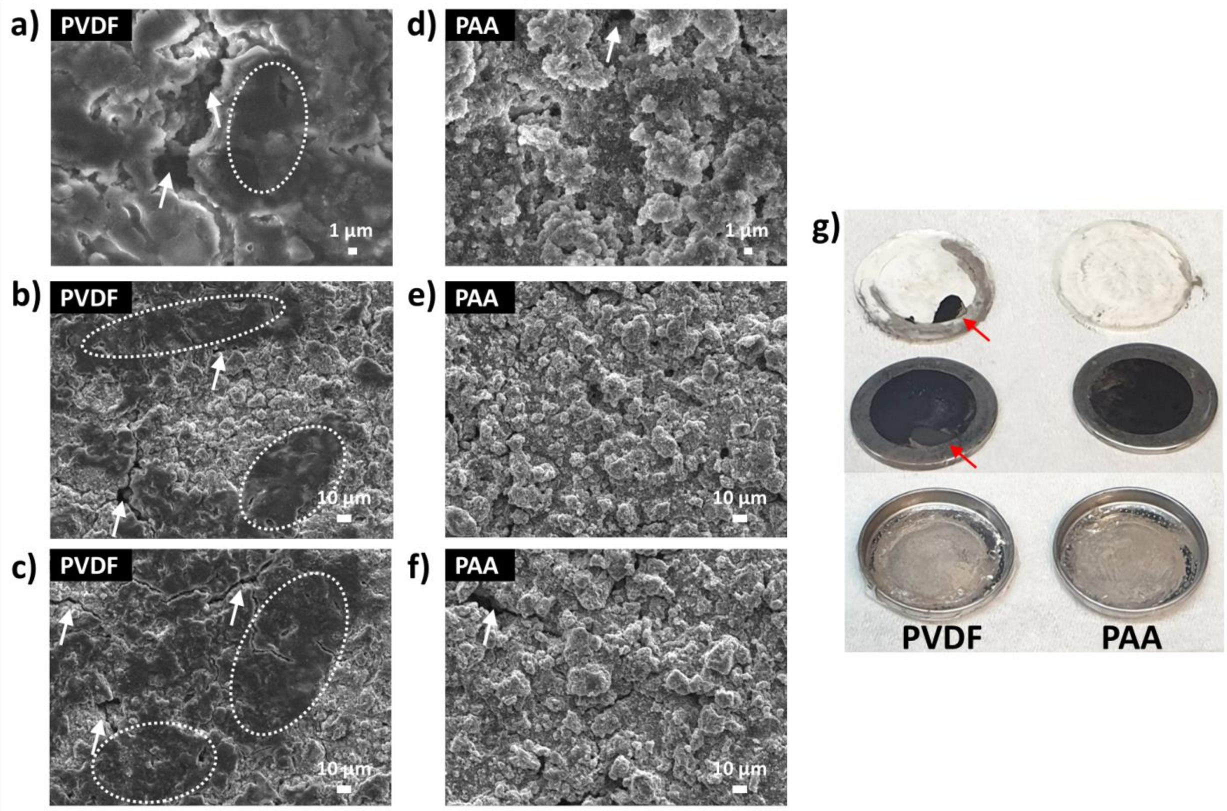

Figure S27. Post-mortem analysis of the cathode architecture after galvanostatic cycling. Additional SEM images of the **a-c)** PVDF cathode and **d-f)** PAA cathode at different magnifications after 50 cycles, at 0.5 C (1 M $NaClO_4$ electrolyte, 1:1 EC/DEC *without* additives). White arrows indicate large cracks in the cathode; dotted ovals denote regions of lower contrast formed as a surface passivation layer. **g)** Images of cycled cell components, top row: separator, middle row: cathode on Al foil current collector, bottom row: sodium anode. Red arrows indicate region of material detachment from the current collector.

Traces of detached material were observed with the PVDF-based cathode, but no staining of the separator had occurred to suggest any dissolution of soluble polysulfide, regardless of the cathode binder. Also, no polysulfide crossover to the Na-anode was detected (Table S9) after extended cycling, due to the S-PAN composite containing only insoluble short-chain sulfur. This demonstrated good polysulfide containment within the cathode structure.

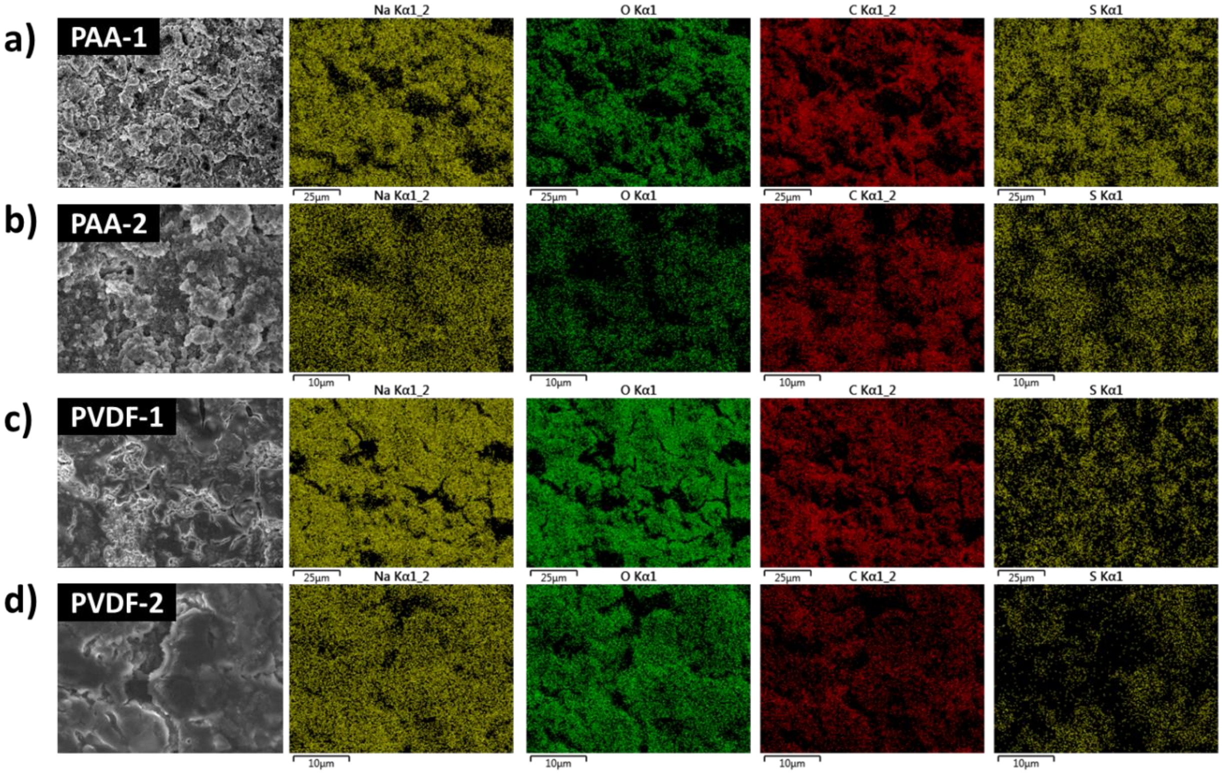

Figure S28. EDX elemental maps of the **a,b)** PAA cathode and **c,d)** PVDF cathode, at varying magnification, after galvanostatic cycling for 50 cycles without electrolyte additives, ending in the charged state.

Table S7. Elemental composition of S-PAN cathodes by energy dispersive X-ray spectroscopy, after extended cycling.

Cathode	**Elemental composition (wt%)**							
	Na	**C**	**O**	**N**	**S**	**Al**	**F**	**Cl**
PAA-1	13.4	50.0	16.5	4.0	13.7	0.0	0.0	2.4
PAA-1	14.2	53.2	14.4	3.9	11.9	0.0	0.0	2.4
PVDF-1	21.1	34.5	31.0	1.1	5.5	0.0	4.0	2.7
PVDF-2	21.4	33.0	34.2	0.5	5.2	0.0	1.3	4.4

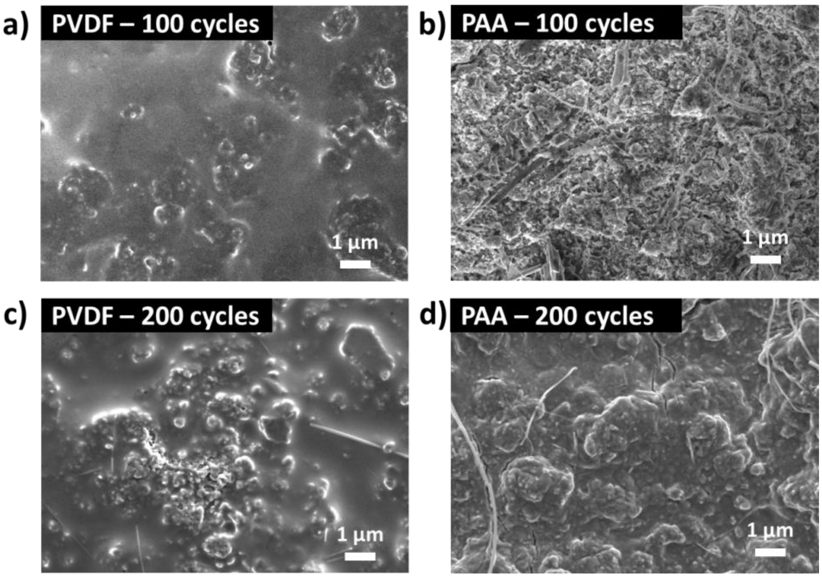

Figure S29. Post-mortem analysis of the cathode architecture after further galvanostatic cycling for 100 and 200 cycles, of the **a,c)** PVDF cathode and **b,d)** PAA cathode. Filament-like structures are from loose glass fibers detached from the separator.

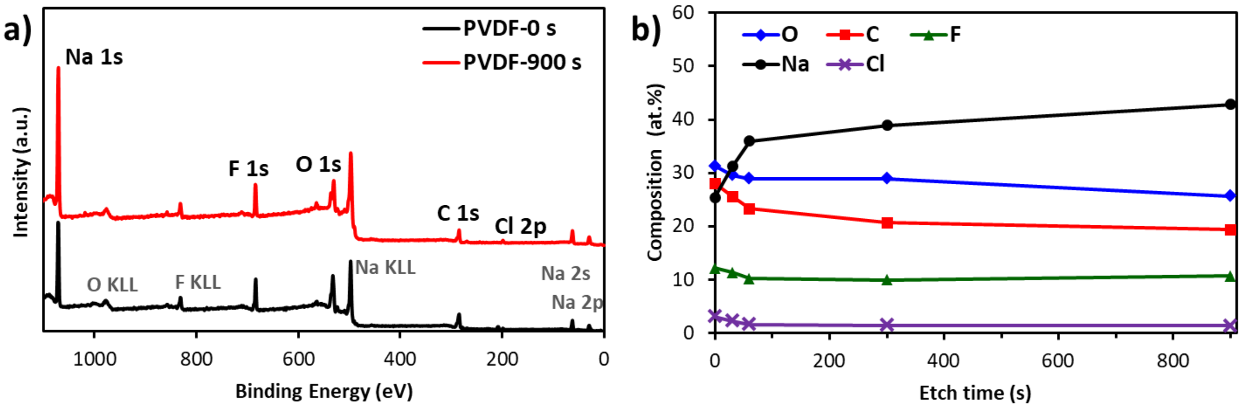

Figure S30. Composition of the surface passivating layer on the PVDF cathode. a) Wide scan X-ray photoelectron spectra of the cycled PVDF cathode (100 cycles) before and after *in-situ* Ar-ion sputtering (2.0 kV, 1.0 mA; estimated etch rate: ~5.5 nm min^{-1}). **b)** Depth profile of the PVDF cathode with increasing etch times.

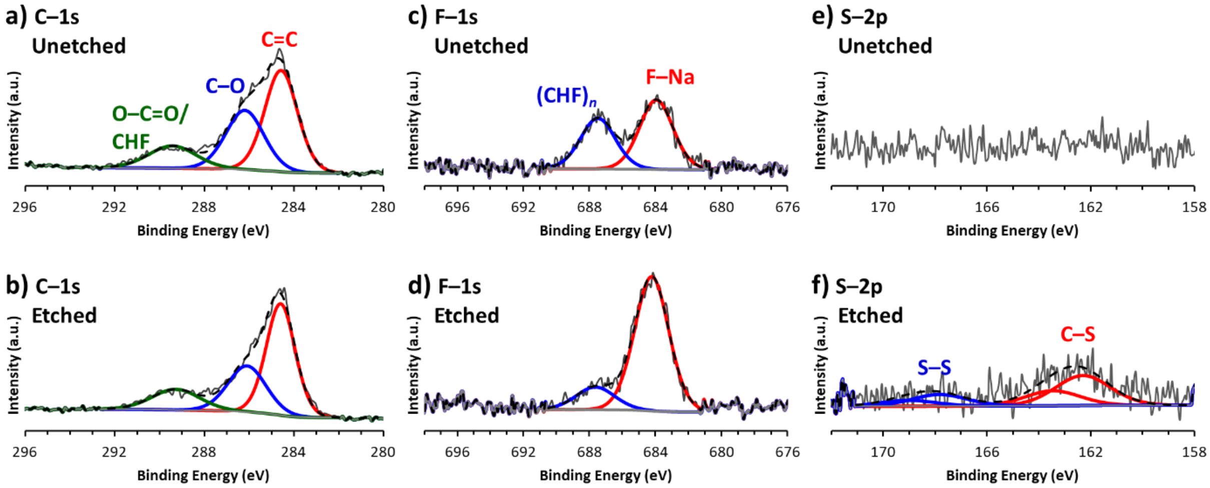

Figure S31. Composition of the surface passivating layer on the PVDF cathode. Deconvoluted high resolution core-level X-ray photoelectron spectra of the cycled PVDF cathode (100 cycles) **a,c,e)** before and **b,d,f)** after Ar-ion sputtering for 600 s. Left panel: carbon-1s region, middle panel: fluorine-1s region, right panel: sulfur-2p region.

Table S8. Bonding information for the surface of the cycled PVDF-based cathode, by X-ray photoelectron spectroscopy, before and after Ar-ion etching.

PVDF cathode/ treatment	**Element / Bonding modes (at.%)**						
	S–2p		**C–1s**			**F–1s**	
	C–S	**S–S**	**C=C**	**C–O**	**C–F/O–C=O**	**F–Na**	**F–C**
Unetched	-	-	50.0	34.0	16.0	57.0	43.0
Etched	72.2	27.8	54.1	29.4	16.5	84.0	16.0

After Ar$^+$ sputtering to etch away the very top surface layers, concentrations of both carbonate (O-C=O, C-O) and fluorocarbon (CHF) species decreased, while the sulfur content increased slightly, thus signifying that the surface passivation layer comprises of decomposed carbonate species from the solvent with the PVDF binder.

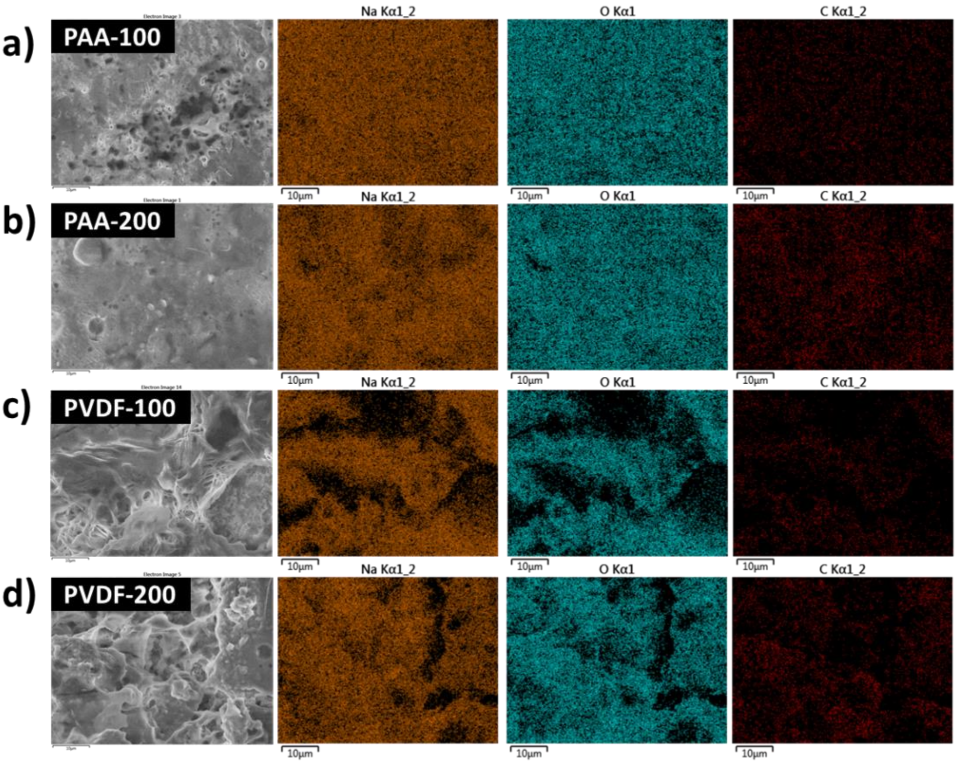

Figure S32. Post-mortem analysis of the unprotected sodium anode, after galvanostatic cycling for 100 and 200 cycles, in the presence of S-PAN cathodes containing **a,b)** PAA and **c,d)** PVDF binders. Electrolyte: 1 M $NaClO_4$ salt in EC:DMC (1:1, *v/v*), *without* electrolyte additives.

Table S9. Elemental composition of cycled sodium anodes by energy dispersive X-ray spectroscopy, after extended cycling.

Sodium anode	**Elemental composition (wt%)**				
	Na	**C**	**O**	**S**	**Cl**
With PAA cathode-100 cycles	48.2	11.4	39.2	0.0	1.1
With PAA cathode-200 cycles	42.5	17.2	38.2	0.0	2.1
With PVDF cathode-100 cycles	46.4	12.2	38.0	0.0	3.4
With PVDF cathode-200 cycles	39.3	16.5	40.2	0.2	3.9

6. Effect of electrolyte additives on stabilization of the Na anode

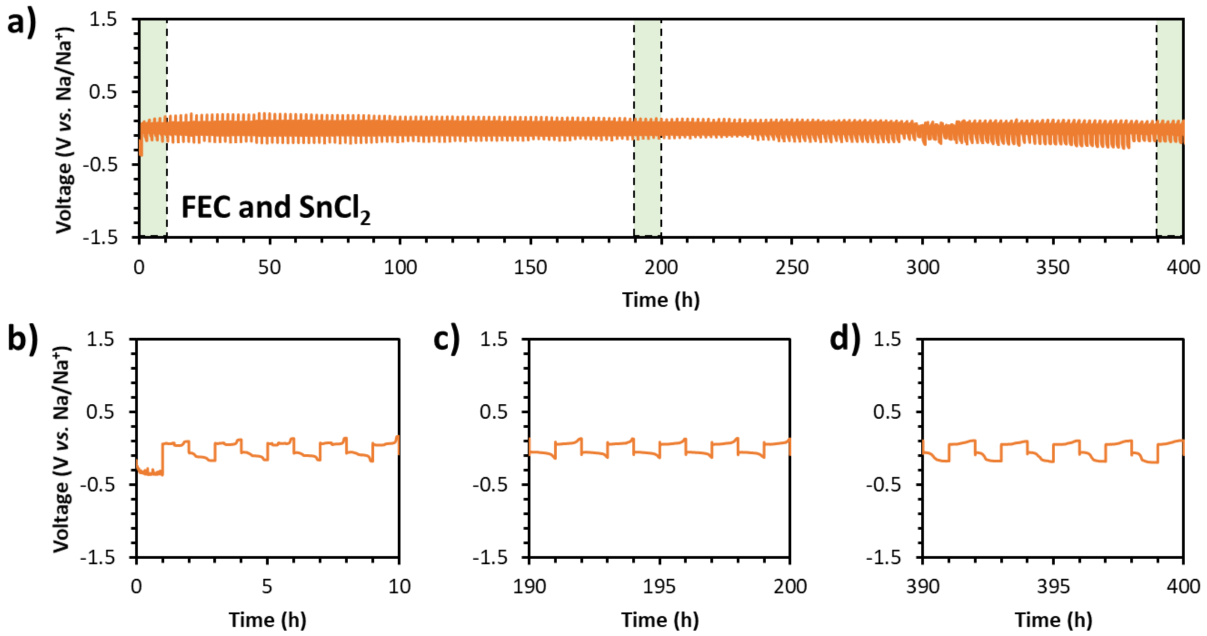

Figure S33. Galvanostatic strip/plating tests of metallic sodium in symmetric cell configuration (Na//Na) at 1 mA cm^{-2} current, with a 1 M $NaClO_4$ electrolyte in EC:DMC (1:1 v/v) containing 40 mM $SnCl_2$ and 8 vol.% FEC additives. Each half-cycle is 1 h; areal capacity is fixed at 1 mAh cm^{-2}.

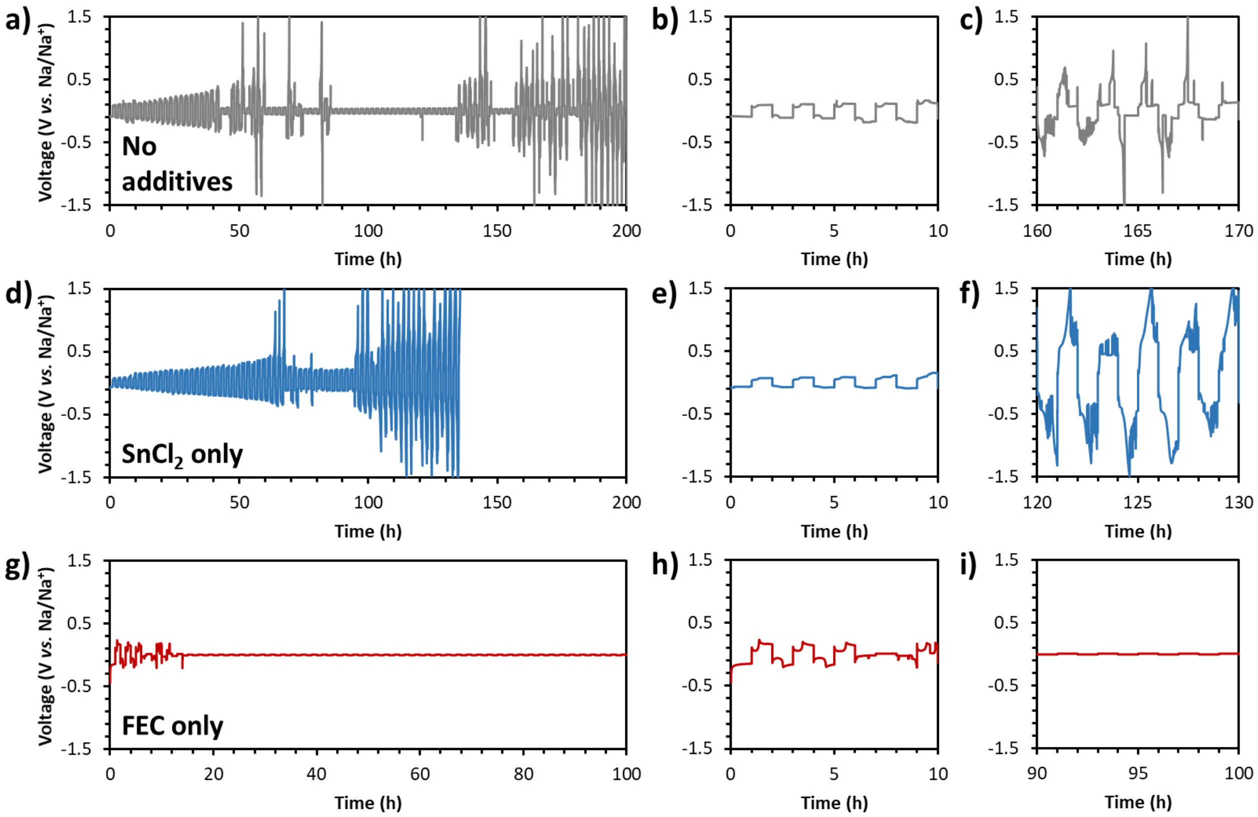

Figure S34. Effects of individual electrolyte additive components on sodium strip-plating. Control galvanostatic strip/plate tests of sodium in symmetric cell configuration at 1 mA cm^{-2} current density, **a)** without electrolyte additives (1 M $NaClO_4$ electrolyte in EC:DMC), **d)** with 40 mM $SnCl_2$ only, and **g)** with 8 vol.% FEC only. Areal capacity is fixed at 1 mAh cm^{-2}. Middle and right panels illustrate initial and subsequent strip/plate cycles, respectively.

The use of either $SnCl_2$ or FEC *alone* as electrolyte additive did not demonstrate any positive effect on sodium-sodium strip-plating. $SnCl_2$ alone similarly resulted in gradually increasing overpotentials as with the control containing no additives. Cells containing only FEC typically did not demonstrate the ability to cycle beyond the first ~10 cycles, due to passivation from the reduction of FEC (Figure S34g). In contrast, a synergistic effect was observed in cells containing both electrolyte additives, demonstrating the ability to cycle stably for over 400 h, maintaining low overpotentials of less than ±0.2 V (Figure S33).

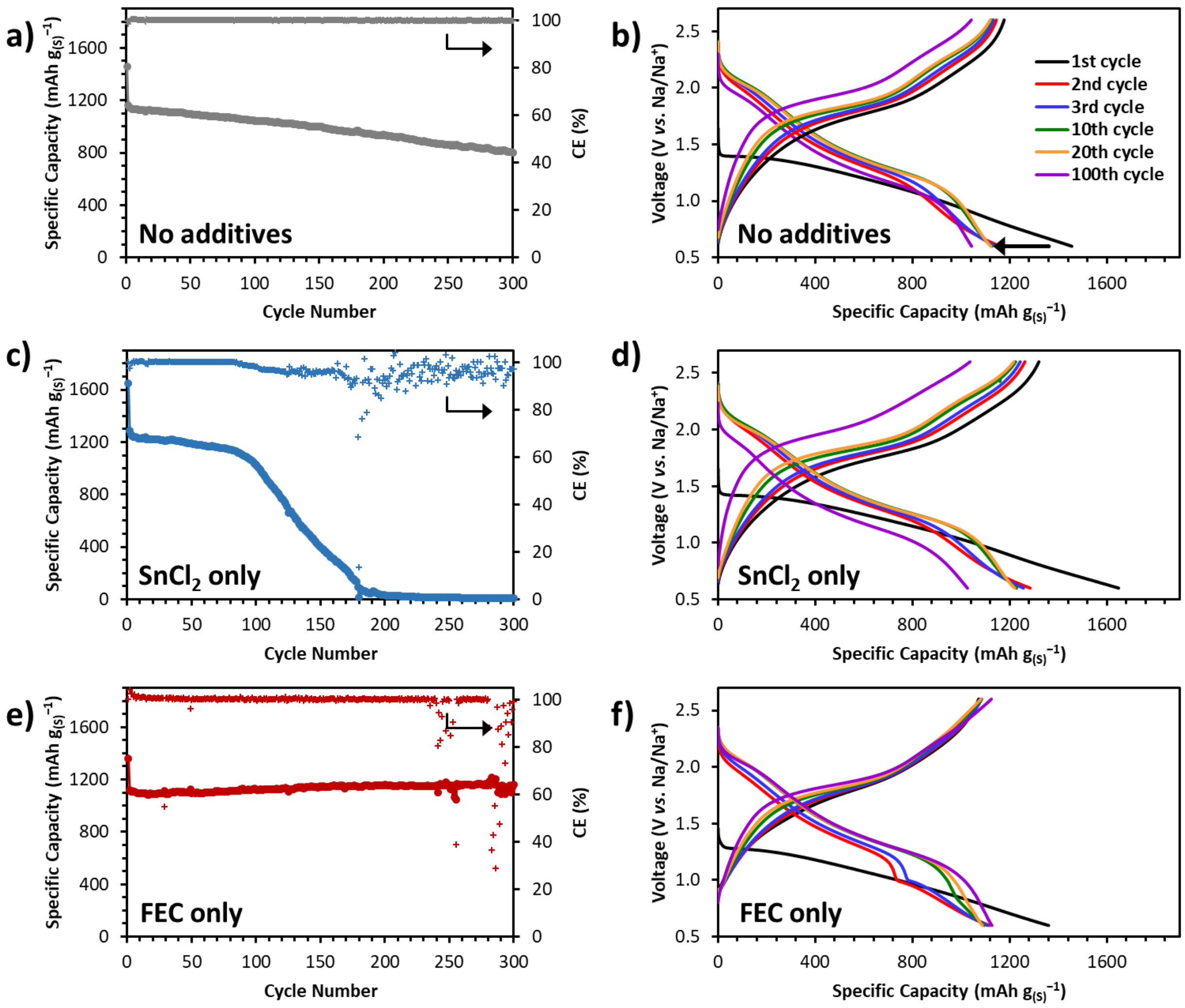

Figure S35. Effects of individual electrolyte additive components on cycling performance. Galvanostatic cycling and Coulombic efficiencies of S-PAN cathodes (PAA binder) at 0.5 C, with a 1 M $NaClO_4$ electrolyte in EC:DMC (1:1 *v/v*) containing **a)** no additives, **c)** $SnCl_2$ only, or **e)** FEC only. **b,d,f)** Corresponding galvanostatic charge/discharge profiles are shown at the right panel. Legend: 1st cycle: black, 2nd cycle: red, 3rd cycle: blue, 10th cycle: green, 20th cycle: orange, 100th cycle: purple. Cycling for sodium-sulfur cells containing both $SnCl_2$ and FEC additives shown in Figure 6 of the main text.

The control experiments corroborate with previous reports on addition of FEC in lithium-sulfur battery systems[5,6] and on sodium metal electrodes.[7] A reduction at *ca.* 1.1 V *vs.* Na/Na$^+$ was observed in early cycles for cells with only FEC (Figure S35f), corresponding to the reduction of FEC at the electrode surface.[2] FEC was also noted to be the main additive component responsible for slowing the *long-term* rate of capacity decline in the sodium-sulfur cell. However, when either $SnCl_2$ or FEC were used alone, they resulted in erratic and unstable Coulombic efficiencies, typically appearing at later charge/discharge cycles.

7. Density Functional Theory Calculations for Binder-Interactions with NaSB Discharge Products

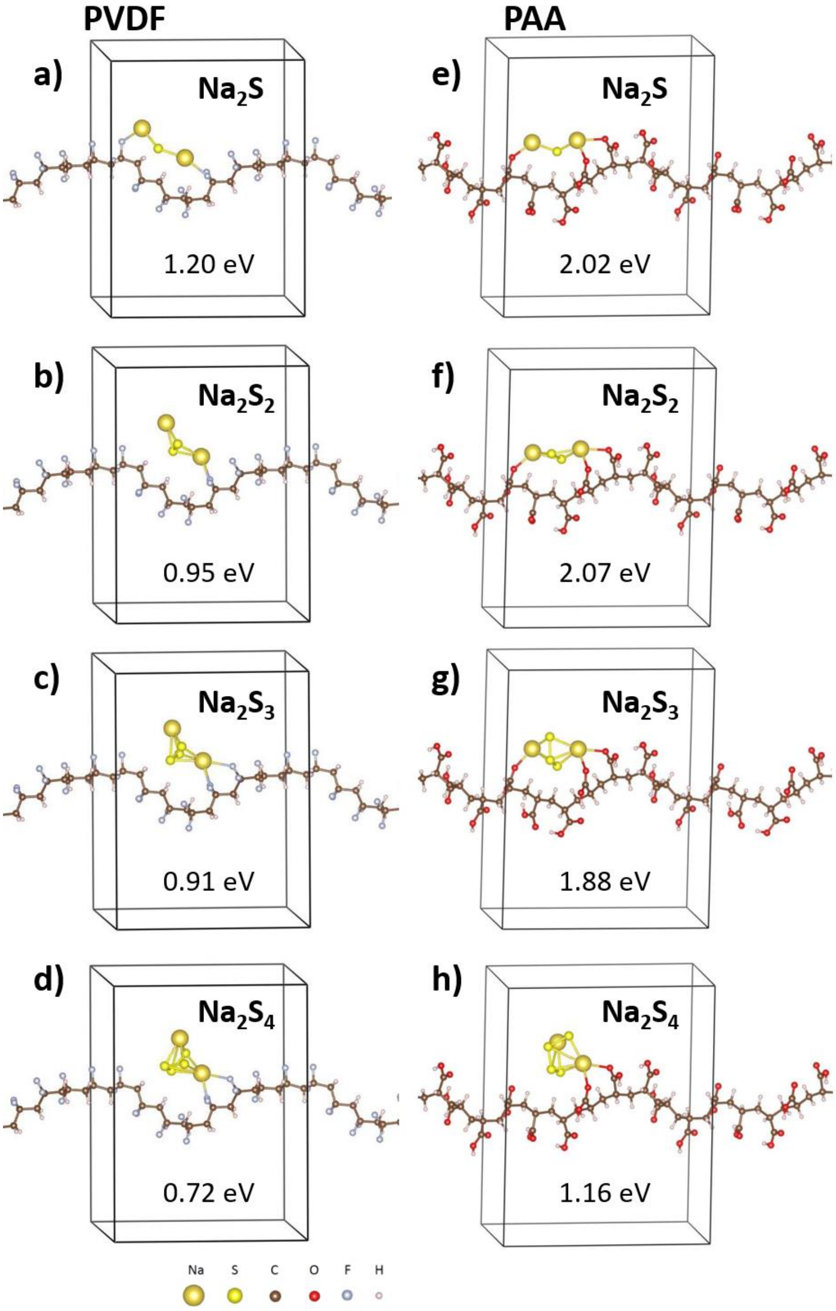

Figure S36. Optimised binding configurations and binding energies of the NaSB discharge product and intermediates with **a-d)** polyvinylidene difluoride $(CF_2–CH_2)_n$, and **e-f)** polyacrylic acid $(CH(COOH)–CH_2)_n$. The polymer shown outside the box is the periodic image.

8. Battery Performance in Ether-based Electrolyte Systems

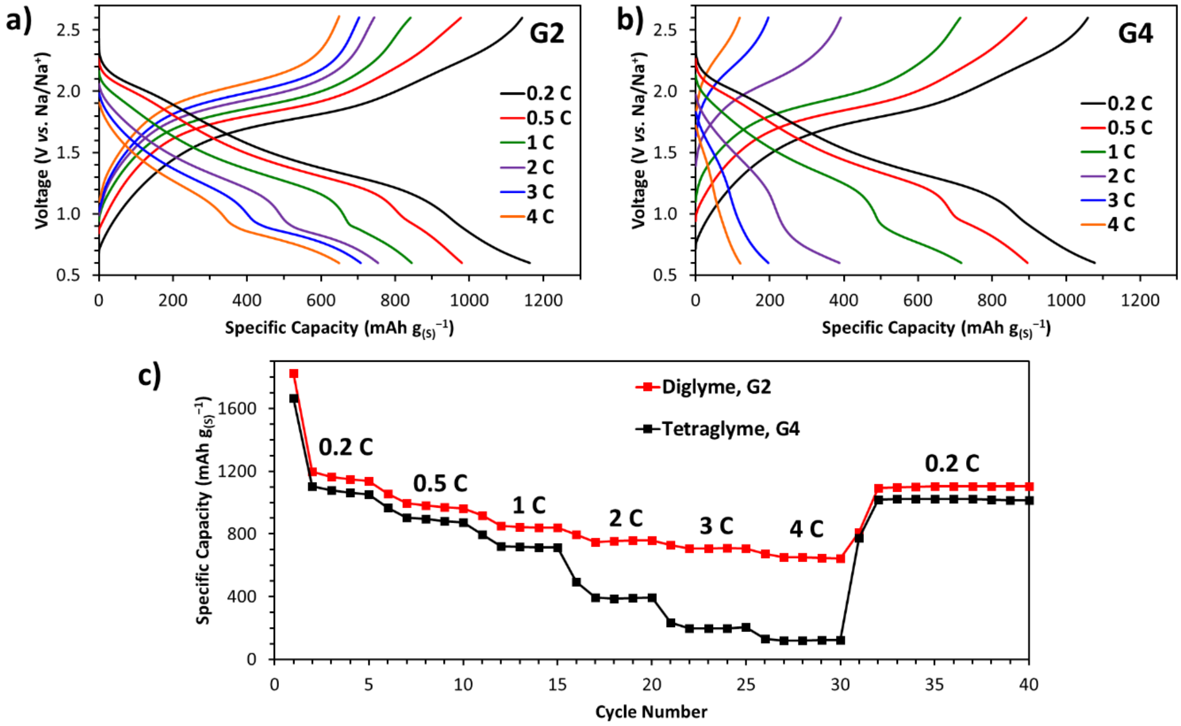

Figure S37. Cycling performances of PAA-binder cathodes with ether-based electrolytes. Galvanostatic charge/discharge profiles at various current densities for NaSBs using **a)** diethylene glycol dimethyl ether (diglyme, G2), and **b)** tetraethylene glycol dimethyl ether (tetraglyme, G4), containing 1 M $NaClO_4$ salt, 40 mM $SnCl_2$, 8 vol.% FEC. **c)** Rate performance for NaSBs utilizing ether-based electrolytes up to 4 C.

A good rate performance was achieved with the diglyme-based electrolyte with a specific capacity of around 650 mAh·$g_{(S)}^{-1}$ maintained at 4 C, while the lower capacity attained with tetraglyme solvent may be attributed to its comparatively higher viscosity.

9. Flexible Cathode with Increased Sulfur Loading

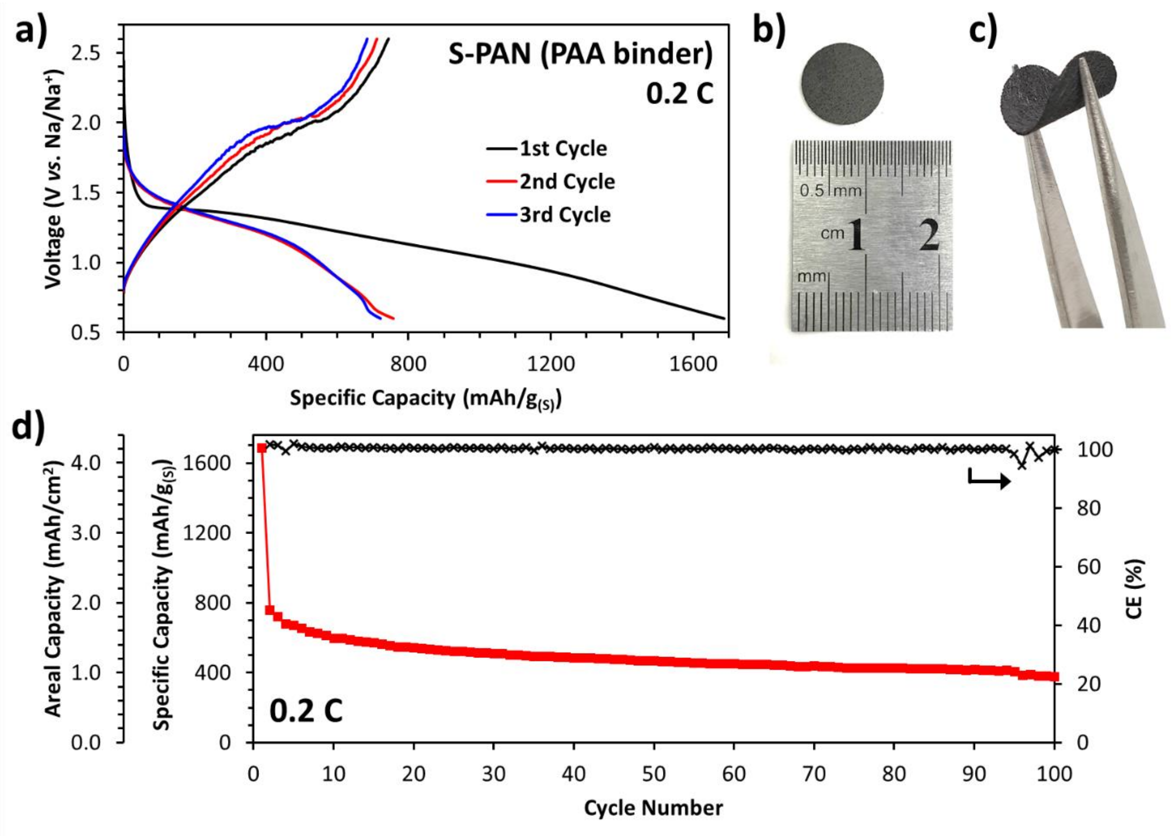

Figure S38. a) Galvanostatic charge/discharge profiles at 0.2 C for a cathode with a high S-PAN loading of 6.5 $mg_{(composite)}/cm^2$, equivalent to 2.5 $mg_{(S)}/cm^2$ as determined from elemental analysis. Electrolyte: 1 M $NaClO_4$ in EC:DMC (1:1 *v/v*) containing 40 mM $SnCl_2$ and 8 vol.% FEC. **b,c)** Images of a flexible carbon paper substrate used as cathode (1 cm^2). Cathodes were prepared by drop-casting a slurry containing 80 wt.% S-PAN, 10 wt.% carbon black, and 10 wt.% PAA binder, with overnight drying under vacuum. **d)** Cycling performance and Coulombic efficiencies at 0.2 C.

Initial specific and areal capacities of *ca*. 760 $mAh/g_{(S)}$ and 1.9 mAh/cm^2 were achieved in the 2nd discharge cycle, with Coulombic efficiencies close to 100% over 100 cycles. Final discharge capacities were maintained at 380 $mAh/g_{(S)}$ and 0.95 mAh/cm^2 respectively at the 100th cycle.

10. Performance Benchmarking for Room-Temperature Sodium-Sulfur Batteries

Energy density calculations: for actual S-PAN (PAA) cell demonstrated in Figure 6d,e

- Approx. capacity of sodium-sulfur cell at 0.2 C
  = initial specific capacity achieved × actual sulfur loading of cathode
  = 1230 mAh/g$_{(S)}$ × 0.76 mg$_{(S)}$
  = 0.935 mAh per cell

- Energy stored in cell
  = cell capacity × approx. mid-point voltage
  = 0.935 mAh × 1.4 V
  = 1.31×10^{-3} Wh

Energy density under optimized conditions,

- Based on composite weight
  = energy stored per cell / S-PAN composite weight
  = 1.31×10^{-3} Wh / 1.84 mg$_{(composite)}$
  ≈ 710 Wh/kg$_{(composite)}$

- Based on total cathode weight, (*i.e.* 70% S-PAN, 20% conductive carbon, 10% binder)
  = energy stored per cell / total cathode weight
  = 1.31×10^{-3} Wh / 2.63 mg$_{(cathode)}$
  ≈ 500 Wh/kg$_{(cathode)}$

Table S10. Comparison of cycling performances of recent NaSB systems, and S-PAN cathodes.

NaSB cathode material	**Specific capacity at max. cycle life (cycle no.)**	**Max. cycle life**	**Capacity loss (per cycle)**	**Sulfur content**	**Reference**
S-PAN particles (*un*doped, PAA-binder enhanced)	**1000 mAh·g^{-1}** (1000th)	**1000**	0.016%	41%	This work, 2020
N-doped carbon/Au/S microspheres	430 mAh·g^{-1} (1000th) 369 mAh·g^{-1} (2000th)	2000	~0.02% – 0.03%	56%	*Energy Environ. Sci.* 2020, **13**, 562
Microporous-carbon sulfur composite	~520 mAh·g^{-1} (500th)	500	0.106%	33%	*Energy Storage Mater.* 2020, **29**, 1.
Microporous-carbon sulfur composite	~495 mAh·g^{-1} (500th)	500	0.09%	33%	*Cell Rep. Phys. Sci.* 2020, **1**, 100044.
Covalent sulfur–carbon complex (SC-BDSA)	452 mAh·g^{-1} (1000th)	1000	0.035%	40%	*Adv. Energy Mater*. 2019, **9**, 1803478
Metal clusters on carbon nanospheres	394 mAh·g^{-1} (1000th)	1000	~0.051%	40%	*Angew. Chem. Int. Ed.* 2019, **58**, 1484.
NiS$_2$ on N-doped carbon	401 mAh·g^{-1} (750th)	750	~0.044%	56%	*Nat. Commun.* 2019, **10**, 4793
Multiporous carbon fiber-sulfur composite	648 mAh·g^{-1} (500th)	500	~0.07%	~60%	*Nat. Commun.* 2018, **9**, 3870.
I-doped S-PAN	768 mAh·g^{-1} (500th)	500	0.045%	42%	*Chem. Commun.* 2019, **55**, 5267
Te-doped S-PAN	970 mAh·g^{-1} (600th)	600	0.015%	41%	*ACS Appl. Energy Mater.* 2019, **2**, 2956
Se-doped S-PAN	770 mAh·g^{-1} (500th)	500	0.045%	44%	*J. Mater. Chem. A* 2019, **7**, 12732
Se-doped S-PAN (electrospun)	800 mAh·g^{-1} (400th)	400	~0.058%	~52%	*Sci. Adv.* 2018, **4**, eaat1687
S-PAN nanowebs (electrospun)	~650 mAh·g^{-1} (200th) 266 mAh·g$_{\mathrm{(composite)}}^{-1}$	200	<0.1%	41%	*J. Power Sources* 2016, **307**, 31
S-PAN fibres (electrospun)	153 mAh·g$_{\mathrm{(composite)}}^{-1}$ (500th)	500	0.06%	31%	*Nano Lett.* 2013, **13**, 4532
S-PAN particles (porous cathode)	500 mAh·g^{-1} (18th)	18	~0.2%	42%	*Electrochem. Commun.* 2007, **9**, 31

Notes: unless otherwise stated, all specific capacities are based on the weight of sulfur, or the combined chalcogen weight in the case of chalcogen-doped S-PAN. Capacity loss is calculated based on the reversible cell capacity (*i.e.* second discharge); irreversible capacities from the first discharge cycles are not considered.

References

---

1. W. Wang, Z. Cao, G. Elia, Y. Wu, W. Wahyudi, E. Abou-Hamad, A. Emwas, L. Cavallo, L. Li and J. Ming, Recognizing the Mechanism of Sulfurized Polyacrylonitrile Cathode Materials for Li–S Batteries and Beyond in Al–S Batteries. *ACS Energy Lett.,* 2018, **3**, 2899-2907.

2. Z. Li, J. Zhang and X. W. Lou, A Pyrolyzed Polyacrylonitrile Selenium Disulfide Composite Cathode with Remarkable Lithium and Sodium Storage Performances. *Sci. Adv.,* 2018, **4**, eaat1687.

3. S. S. Zhang, Understanding of Sulfurized Polyacrylonitrile for Superior Performance Lithium/Sulfur Battery. *Energies,* 2014, **7**, 4588–4600.

4. Z. Li, L. Yuan, Z. Yi, Y. Liu. and Y. Huang, Confined Selenium Within Porous Carbon Nanospheres As Cathode for Advanced Li–Se Batteries. *Nano Energy,* 2014, **9**, 229–236.

5. H. M. Kim, J.-Y. Hwang, D. Aurbach and Y.-K. Sun. Electrochemical Properties of Sulfurized-Polyacrylonitrile Cathode for Lithium−Sulfur Batteries: Effect of Polyacrylic Acid Binder and Fluoroethylene Carbonate Additive. *J. Phys. Chem. Lett.,* 2017, **8**, 5331−5337.

6. X. Xu, D. Zhou, X. Qin, K. Lin, F. Kang, B. Li, D. Shanmukaraj, T. Rojo, M. Armand and G. Wang, A Room-Temperature Sodium-Sulfur Battery with High Capacity and Stable Cycling Performance. *Nat. Commun.,* 2018, **9**, 3870.

7. Y. Lee, J. Lee, J. Lee, K. Kim, A. Cha, S. Kang, T. Wi, S. Kang, H. Lee and N. Choi, Fluoroethylene Carbonate-Based Electrolyte with 1 M Sodium Bis(fluorosulfonyl)imide Enables High-Performance Sodium Metal Electrodes. *ACS Appl. Mater. Interfaces,* 2018, **10**, 15270-15280.